J. Fluid Mech. (2009), *vol.* 640, *pp.* 27–54.
doi:10.1017/S0022112009991212

Motion of a drop along the centreline of a capillary in a pressure-driven flow

ETIENNE LAC†[1] AND J. D. SHERWOOD[2]

[1] Schlumberger-Doll Research, One Hampshire Street, Cambridge MA 02139-1578, USA

[2] Department of Applied Mathematics and Theoretical Physics, University of Cambridge, Wilberforce Road, Cambridge CB3 0WA, UK

(Received 30 May 2008; revised 10 July 2009; accepted 16 July 2009; first published online 2 November 2009)

The deformation of a drop as it flows along the axis of a circular capillary in low Reynolds number pressure-driven flow is investigated numerically by means of boundary integral computations. If gravity effects are negligible, the drop motion is determined by three independent parameters: the size a of the undeformed drop relative to the radius R of the capillary, the viscosity ratio λ between the drop phase and the wetting phase and the capillary number Ca, which measures the relative importance of viscous and capillary forces. We investigate the drop behaviour in the parameter space $(a/R, \lambda, Ca)$, at capillary numbers higher than those considered previously. If the fluid flow rate is maintained, the presence of the drop causes a change in the pressure difference between the ends of the capillary, and this too is investigated. Estimates for the drop deformation at high capillary number are based on a simple model for annular flow and, in most cases, agree well with full numerical results if $\lambda \geqslant 1/2$, in which case the drop elongation increases without limit as Ca increases. If $\lambda < 1/2$, the drop elongates towards a limiting non-zero cylindrical radius. Low-viscosity drops ($\lambda < 1$) break up owing to a re-entrant jet at the rear, whereas a travelling capillary wave instability eventually develops on more viscous drops ($\lambda > 1$). A companion paper (Lac & Sherwood, *J. Fluid Mech.*, doi:10.1017/S002211200999156X) uses these results in order to predict the change in electrical streaming potential caused by the presence of the drop when the capillary wall is charged.

1. Introduction

The main aim of the work presented here and in a second paper (Lac & Sherwood 2009) is to determine how the presence of a liquid drop disturbs the electrical streaming potential generated by pressure-driven flow through a capillary with charged walls. We shall assume that the electric fields generated by the flow are sufficiently small that perturbations to the flow field due to electric stresses are negligible. The first step of the computation is therefore to determine the hydrodynamic behaviour of a drop as it flows through the capillary, in the absence of any electrical effects. This problem is of sufficient importance in its own right that it is discussed separately in this first paper. Electrokinetic effects will be considered by Lac & Sherwood (2009).

The motion of a drop in a straight capillary represents an idealized two-phase flow in a porous medium: the geometry of a realistic porous material (e.g. rock)

† Email address for correspondence: elac@slb.com

is much more complex. The presence of the drop is known to modify the pressure difference necessary to maintain a given flow rate, or equivalently, the flow rate driven by a constant pressure difference (Olbricht 1996). We compute the flow field due to the motion of the drop in the capillary at a given steady flow rate, assuming creeping flow conditions. The motion and deformation of a drop in a pressure-driven flow is a classical hydrodynamic problem. Experimental data (e.g. Ho & Leal 1975; Olbricht & Kung 1992) and analytical models (e.g. Goldsmith & Mason 1963; Greenstein & Happel 1968; Hyman & Skalak 1972; Hodges, Jensen & Rallison 2004) are available in the literature. Computations of the motion of a drop in a capillary have also been reported, using finite-element techniques (e.g. Westborg & Hassager 1989; Edvinsson & Irandoust 1996) or the boundary integral method (Martinez & Udell 1990; Tsai & Miksis 1994). Nonetheless, little is known about the drop behaviour at large capillary numbers. Our work confirms some of the earlier studies cited above, and we present new computational results for highly elongated drops in pressure-driven flow at higher capillary numbers than those previously studied.

The governing equations for the hydrodynamics are set down in § 2; in particular, the boundary integral equations used to determine the inertialess flow field are given in § 2.2. Section 3 presents our numerical method for deformable drops of arbitrary size and for spherical drops of infinite surface tension fitting in the tube. We first present asymptotic predictions for long slender drops moving along the centreline of the capillary (§ 4). Numerical results for deformable drops of arbitrary size follow in § 5, and instabilities at high capillary numbers are reported in § 6.

2. Governing equations

2.1. *Hydrodynamics*

We consider the motion of a liquid drop in a cylindrical capillary of radius R filled with another liquid. The drop consists of an incompressible Newtonian liquid of dynamic viscosity $\bar{\mu}$, density $\bar{\rho}$ and volume $\mathscr{V}$; its size is characterized by the radius a of the sphere of the same volume $\mathscr{V} = \frac{4}{3}\pi a^3$. The suspending liquid has dynamic viscosity μ and density $\rho = \bar{\rho}$ identical to that of the drop, so that the drop is neutrally buoyant. The coefficient of interfacial tension between the two phases is denoted by γ. Fluid flows at constant volumetric flow rate $\pi R^2 U$ under the action of a pressure gradient along the capillary.

In the absence of the drop, the (single-phase) flow reduces to a Poiseuille flow, with

$$U = -\frac{R^2 G_0}{8\mu}, \tag{2.1}$$

where G_0 is the (uniform) pressure gradient. The boundaries of the domain are the entrance and exit sections $\mathscr{S}_{in}$ and $\mathscr{S}_{out}$, the solid surface of the capillary $\mathscr{S}_w$ and the drop/medium interface $\mathscr{S}$, as depicted in figure 1. Note that, hereafter, barred variables refer to the drop phase.

The Reynolds number $Re = \rho R U/\mu$ is usually small in flow through low permeability porous media. Accordingly, we assume that the motion of both fluids is governed by the Stokes equations:

$$\nabla \cdot \boldsymbol{u} = 0 \qquad \text{(resp. } \bar{\boldsymbol{u}}\text{)}, \tag{2.2a}$$

$$\mu \nabla^2 \boldsymbol{u} = \nabla P - \rho \boldsymbol{g} = \nabla p \qquad \text{(resp. } \bar{\mu}, \bar{\boldsymbol{u}}, \bar{P}, \bar{\rho}, \bar{p}\text{)}, \tag{2.2b}$$

where $\boldsymbol{u}$, P and $\boldsymbol{g}$ denote the velocity, pressure and acceleration due to gravity, respectively, and the modified pressure $p = P - \rho \boldsymbol{x} \cdot \boldsymbol{g}$ includes the gravitational body force.

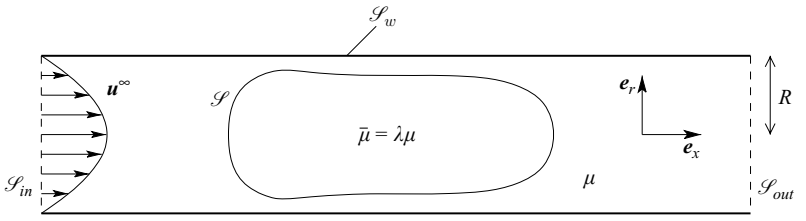

FIGURE 1. Representation of a drop suspended in a pressure-driven flow.

We assume that the wetting phase satisfies a no-slip condition at the capillary wall

$$\boldsymbol{u}(\boldsymbol{x}) = \boldsymbol{0}, \qquad \forall\, \boldsymbol{x} \in \mathscr{S}_w. \tag{2.3}$$

Far behind and ahead of the drop, the outer flow reduces to a Poiseuille flow, since the flow perturbation generated by a point-force distribution decays exponentially down and upstream (Liron & Shahar 1978). We assume that the cross-sections $\mathscr{S}_{in}$ and $\mathscr{S}_{out}$ are sufficiently far from the drop that the flow perturbation has already vanished, and so the boundary conditions at the ends of the capillary are

$$\boldsymbol{u}(\boldsymbol{x}) = \boldsymbol{u}^\infty(\boldsymbol{x}) = 2U\left(1 - \frac{r^2}{R^2}\right)\boldsymbol{e}_x \qquad \forall\, \boldsymbol{x} \in \mathscr{S}_{in} \cup \mathscr{S}_{out}, \tag{2.4a}$$

$$\boldsymbol{\sigma}(\boldsymbol{x})\cdot\boldsymbol{n} = -p_{in}\,\boldsymbol{e}_x - 4\,\frac{\mu U r}{R^2}\,\boldsymbol{e}_r \qquad \forall\, \boldsymbol{x} \in \mathscr{S}_{in}, \tag{2.4b}$$

$$\boldsymbol{\sigma}(\boldsymbol{x})\cdot\boldsymbol{n} = p_{out}\,\boldsymbol{e}_x + 4\,\frac{\mu U r}{R^2}\,\boldsymbol{e}_r \qquad \forall\, \boldsymbol{x} \in \mathscr{S}_{out}, \tag{2.4c}$$

where (x, r, φ) denote cylindrical coordinates with unit basis vectors $(\boldsymbol{e}_x, \boldsymbol{e}_r, \boldsymbol{e}_\varphi)$, $\boldsymbol{n}$ is the unit normal vector pointing inward into the suspending liquid and $\boldsymbol{\sigma}$ is the Newtonian stress tensor with respect to p.

On any point $\boldsymbol{x}$ of the drop interface $\mathscr{S}$, kinematic and dynamic conditions are

$$\boldsymbol{u}(\boldsymbol{x}) = \bar{\boldsymbol{u}}(\boldsymbol{x}) = \frac{\partial \boldsymbol{x}}{\partial t}\,, \tag{2.5a}$$

$$\Delta\boldsymbol{f} = 2\kappa\gamma\,\boldsymbol{n}\,, \tag{2.5b}$$

where $\Delta\boldsymbol{f} = (\boldsymbol{\sigma} - \bar{\boldsymbol{\sigma}})\cdot\boldsymbol{n}$ is the jump of viscous traction across the interface and κ denotes the mean curvature of the surface.

2.2. *Boundary integral formulation*

Taking into account the continuity of the velocity field (2.5*a*), the Stokes problem (2.2) may be formulated as a boundary integral equation (Pozrikidis 1992), where the velocity $\boldsymbol{u}$ at point $\boldsymbol{x}$ is given by

$$\begin{aligned} 4\pi\beta\,\boldsymbol{u}(\boldsymbol{x}) = {} & \oint_{\partial\Omega} \boldsymbol{J}(\boldsymbol{x},\boldsymbol{y})\cdot\boldsymbol{f}(\boldsymbol{y})\,\mathrm{d}S(\boldsymbol{y}) + \mu\oint_{\partial\Omega} \boldsymbol{u}(\boldsymbol{y})\cdot\boldsymbol{K}(\boldsymbol{x},\boldsymbol{y})\cdot\boldsymbol{n}(\boldsymbol{y})\,\mathrm{d}S(\boldsymbol{y}) \\ & - \oint_{\mathscr{S}} \boldsymbol{J}(\boldsymbol{x},\boldsymbol{y})\cdot\Delta\boldsymbol{f}(\boldsymbol{y})\,\mathrm{d}S(\boldsymbol{y}) + (\mu - \bar{\mu})\oint_{\mathscr{S}} \boldsymbol{u}(\boldsymbol{y})\cdot\boldsymbol{K}(\boldsymbol{x},\boldsymbol{y})\cdot\boldsymbol{n}(\boldsymbol{y})\,\mathrm{d}S(\boldsymbol{y}). \end{aligned} \tag{2.6}$$

In (2.6), $\partial\Omega \equiv \mathscr{S}_{in} \cup \mathscr{S}_{out} \cup \mathscr{S}_w$, $\boldsymbol{f}$ represents the viscous stress $\boldsymbol{\sigma}\cdot\boldsymbol{n}$ at the boundary $\partial\Omega$, $\boldsymbol{n}$ is the unit normal vector pointing inward into the suspending liquid and $\Delta\boldsymbol{f}$ is defined by (2.5*b*); $\boldsymbol{J}$ and $\boldsymbol{K}$ are the free-space Green's functions given, in Cartesian

coordinates, by

$$J_{ij}(\boldsymbol{x}, \boldsymbol{y}) = \frac{\delta_{ij}}{\hat{r}} + \frac{\hat{r}_i \hat{r}_j}{\hat{r}^3} \quad \text{and} \quad K_{ijk}(\boldsymbol{x}, \boldsymbol{y}) = -6 \frac{\hat{r}_i \hat{r}_j \hat{r}_k}{\hat{r}^5}, \tag{2.7}$$

with $\hat{\boldsymbol{r}} = \boldsymbol{y} - \boldsymbol{x}$ and $\hat{r} = |\hat{\boldsymbol{r}}|$. The value of β in (2.6) depends on the position of $\boldsymbol{x}$; in particular,

$$\beta = \begin{cases} \mu + \bar{\mu} & \text{if } \boldsymbol{x} \in \mathscr{S}, \\ \mu & \text{if } \boldsymbol{x} \in \partial\Omega. \end{cases} \tag{2.8}$$

According to the set of boundary conditions (2.3)–(2.5), the unknowns of (2.6) are the interfacial velocity $\boldsymbol{u}$ on $\mathscr{S}$, the viscous stress at the wall $\boldsymbol{f}^w$ and the pressures p_{in} and p_{out}. Adding a constant pressure in the stress field does not change the formulation (2.6), since

$$\oint_{\partial D} \boldsymbol{J}(\boldsymbol{x}, \boldsymbol{y}) \cdot \boldsymbol{n}(\boldsymbol{y}) \, \mathrm{d}S(\boldsymbol{y}) = \boldsymbol{0} \tag{2.9}$$

for any domain D and any point $\boldsymbol{x}$ in space. Consequently, we may impose arbitrarily p_{in} or p_{out}, and only the difference

$$\Delta p = p_{in} - p_{out} \tag{2.10}$$

is unknown. For simplicity, we set $p_{in} = 0$, and seek p_{out}. Furthermore, since the pressure at $\mathscr{S}_{out}$ yields the normal stress on the wall at the end of the capillary, p_{out} may be replaced by $-f_r^w(\boldsymbol{x} \in \mathscr{S}_{out})$ in (2.6), which shortens the list of unknowns to the velocity $\boldsymbol{u}$ on the drop interface and the stress distribution $\boldsymbol{f}^w$ at the capillary wall.

In the absence of any drop, the pressure difference required for Poiseuille flow along a capillary of length L_w is

$$\Delta p_0 = -G_0 L_w = \frac{8\mu U L_w}{R^2}. \tag{2.11}$$

In addition to finding the drop shape and velocity, we shall also be interested in the additional pressure drop

$$\Delta p_a = \Delta p - \Delta p_0 \tag{2.12}$$

necessary to maintain the volumetric flow rate $\pi R^2 U$ in the presence of the drop.

2.3. *Dimensional analysis*

Natural scales for lengths and velocities are the radius R of the capillary and the mean velocity U of the imposed flow, respectively. A convenient scale for stress is then the typical viscous stress $\mu U/R$, and time is naturally scaled by R/U. The interface stress balance (2.5*b*) reveals the importance of the viscosity ratio $\lambda = \bar{\mu}/\mu$ and the capillary number

$$Ca = \frac{\mu U}{\gamma}, \tag{2.13}$$

which compares the magnitude of viscous stresses with interfacial tension.

Hence, the hydrodynamic problem has three independent parameters: the relative size of the drop $\alpha = a/R$, the viscosity ratio λ and the capillary number Ca. Note that hereafter, an asterisk denotes a dimensionless quantity, according to the scaling proposed above.

3. Numerical method

3.1. *Discretization of the problem*

If we consider axisymmetric configurations only, the surface integrals in (2.6) can be analytically calculated in the azimuthal direction in terms of elliptic integrals (Pozrikidis 1992, § 2.4). Consequently, surface integrals reduce to line integrals along the profile of the different boundaries, and only these profiles need to be discretized.

The drop profile is divided into N elements defining $N+1$ nodes $(\boldsymbol{x}^0, \ldots, \boldsymbol{x}^N)$, where the two extreme nodes lie on the axis of revolution. Between two neighbouring nodes, the interface is interpolated with a cubic B-spline:

$$\boldsymbol{x}(\xi, t) = \sum_{k=-1}^{N+1} \check{\boldsymbol{x}}_k(t)\, B_k(\xi), \tag{3.1}$$

where the B_k are piecewise cubic polynomials and $\check{\boldsymbol{x}}_k$ are the spline coefficients associated with $\boldsymbol{x}$ at time t. The parameter ξ runs from 0 to 1, such that $\xi = 0$ and $\xi = 1$ correspond to the nodes $\boldsymbol{x}^0$ and $\boldsymbol{x}^N$, respectively. For each scalar variable, the spline representation (3.1) requires $N+3$ spline coefficients and two boundary conditions imposed on the axis of revolution. For a variable that vanishes on the axis owing to the axisymmetry of the problem (such as the radial component of any vector field), we impose that the second derivative with respect to ξ be zero at $\boldsymbol{x}^0$ and $\boldsymbol{x}^N$. Otherwise, we require the first derivative to be zero.

The capillary wall is discretized in a similar fashion with N_w elements, but the two extreme wall nodes $\boldsymbol{x}_w^0$ and $\boldsymbol{x}_w^{N_w}$ are, respectively, located on the entrance and exit sections, where boundary conditions are imposed. These sections are located at a distance $x = \pm L_w/2$ from the drop centre of mass, so the tube has a total length $L_w = O(10\,R)$. Note that since N_w is *a priori* different from N, a separate set of N_w+3 basis functions $B_k^w(\xi)$ must be calculated.

In the spline coefficient space, the integral equation (2.6) yields a linear system of size $2(N+3)+2(N_w+3)$, which we solve using the open-source library Lapack. Part of this linear system is built with $2(N+1)$ equations provided by the two components of (2.6) at $\boldsymbol{x} = \boldsymbol{x}^j$ along the drop profile ($j = 0, \ldots, N$), and by appropriate boundary conditions for $\boldsymbol{u}$ on the axis of revolution. The rest of the system is calculated similarly by choosing $\boldsymbol{x} = \boldsymbol{x}_w^j$ ($j = 1, \ldots, N_w - 1$), together with seven equations given by the boundary conditions:

$$\begin{aligned}
&\text{for } \boldsymbol{x} \in \mathscr{S}_w \cap \mathscr{S}_{in}, \quad f_x^w = -\frac{4\mu U}{R}, \quad \frac{\partial f_x^w}{\partial x} = 0, \quad f_r^w = -p_{in} = 0, \quad \frac{\partial^2 f_r^w}{\partial x^2} = 0;\\
&\text{for } \boldsymbol{x} \in \mathscr{S}_w \cap \mathscr{S}_{out}, \quad f_x^w = -\frac{4\mu U}{R}, \quad \frac{\partial f_x^w}{\partial x} = 0, \quad \frac{\partial^2 f_r^w}{\partial x^2} = 0.
\end{aligned} \tag{3.2}$$

The missing equation is indifferently given by either component of (2.6) for $\boldsymbol{x}$ in $\mathscr{S}_{in}$; we place this point on the axis for convenience and use the x component of (2.6).

When the drop and the outer liquid have the same dynamic viscosity ($\lambda = 1$), (2.6) simplifies because the double-layer integral over $\mathscr{S}$, containing the unknown $\boldsymbol{u}$, disappears. In this particular case, a separated integral equation may be written for $\boldsymbol{f}^w$ by picking $\boldsymbol{x}$ on $\partial\Omega$, since $\boldsymbol{u}$ is known everywhere on $\partial\Omega$ ((2.3) and (2.4*a*)). The size of the linear system to be solved is then $2(N_w+3)$. Once $\boldsymbol{f}^w$ is determined, (2.6) with $\lambda = 1$ allows for a direct calculation of $\boldsymbol{u}(\boldsymbol{x})$ on $\mathscr{S}$.

The drop interface is convected according to

$$\frac{\partial \boldsymbol{x}}{\partial t} = u_n(\boldsymbol{x})\,\boldsymbol{n}(\boldsymbol{x}), \tag{3.3}$$

where $\boldsymbol{x}$ is an interface node and $u_n = \boldsymbol{u}\cdot\boldsymbol{n}$ is given by (2.6). At each time step, the interface is re-meshed to ensure a denser distribution of nodes in high-curvature regions. Owing to the imposed flow rate $\pi R^2 U$, the drop is convected downstream along the capillary. In order to simulate an infinitely long tube, we subtract at each time step the velocity of the drop centre of mass $\boldsymbol{V} = V\,\boldsymbol{e}_x$ from the velocity field, which is equivalent to replacing u_n by $u_n' = u_n - \boldsymbol{V}\cdot\boldsymbol{n}$ in (3.3). This process does not affect the stress field and, therefore, does not influence the drop shape. Evidently, it is valid only for a straight cylindrical capillary, the shape of which remains unchanged as the drop is re-centred.

Equation (3.3) is solved numerically by a second- or fourth-order Runge–Kutta method, depending on the desired accuracy. A satisfactory steady state is obtained when the maximum absolute normal velocity $|u_n'|/U$ on $\mathscr{S}$ is smaller than a chosen tolerance ($\sim 10^{-5}$, typically).

The flow is suddenly started at time $t = 0$, with a flow strength characterized by Ca. If the drop is sufficiently small to fit undeformed in the tube without touching the wall ($a < R$), its initial shape is spherical. Otherwise, we place in the flow a spheroidal drop of volume $\frac{4\pi}{3}a^3$ and breadth $R_i < R$ (we arbitrarily choose $R_i = 0.95\,R$). If the flow strength is abruptly modified at $t = t_0$ from Ca_1 to Ca_2, we usually start the simulation from the steady drop shape (if any) obtained at Ca_1.

In our simulations, N ranges from 50 to 256, and N_w from 100 to 400, depending on the tube length (which itself depends upon the drop volume). To maintain numerical stability, the dimensionless time step Δt^* (scaled by R/U) has to be sufficiently small owing to the explicit numerical resolution of the advection equation (3.3); the maximum stable value of Δt^* decreases as either α, Ca or λ decreases, and as N increases. Since the velocity given by (2.6) is divergence-free, the change in the drop volume during simulations gives an estimate of the accuracy of the computations. We observed in the worst cases a maximum relative volume variation of order of 10^{-4} over a full simulation ($\sim 10^3$–10^5 time steps). These cases usually correspond to large drops ($\alpha \geqslant 1.5$), small capillary numbers ($Ca \sim 10^{-2}$) and large viscosity contrasts (λ^{-1} or $\lambda \gg 1$), since $\lambda = 0$ and $\lambda \to \infty$ correspond to eigenvalues of (2.6); it is possible to remove these eigenvalues (see § 4.6 of Pozrikidis 1992), though we have not implemented this method here. We show in figure 2(*a*) the typical volume variation observed for two discretizations: $N = 50$ and $N = 125$. We also plot the time evolution of the maximum normal velocity in the frame of reference moving with the drop, expected to vanish at steady state (figure 2*b*), and observe that the final steady drop shape is independent of N (figure 2*c*).

3.2. *The mobility problem for spherical drops*

The limit $Ca = 0$ corresponds to an infinitely large interfacial tension that prevents deformation of the drop by the flow. This case cannot be tackled by the method described above because the condition (2.5*b*) is undetermined. Instead, we assume that the drop shape is known, and treat the stress distribution $\Delta\boldsymbol{f}$ as an additional unknown to be determined. Note that this approach is valid only when $a < R$, i.e. when the spherical drop fits within the tube. Since the tangential viscous stress is

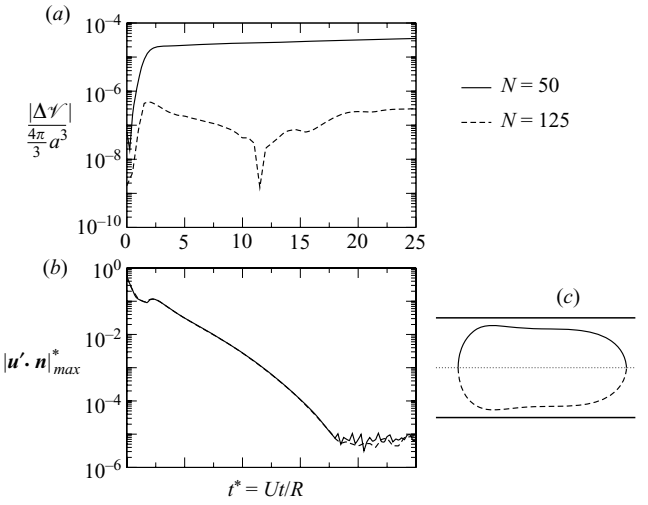

FIGURE 2. (*a*) Drop volume variation $\Delta\mathscr{V} = \mathscr{V} - \frac{4\pi}{3}a^3$ and (*b*) maximum normal velocity $|\boldsymbol{u}'\cdot\boldsymbol{n}|$ ($\boldsymbol{u}' = \boldsymbol{u} - V\boldsymbol{e}_x$) as a function of time; (*c*) steady drop profile at $t^* = 25$. Two drop discretizations, $N = 50, 125$; $\alpha = 1.1$, $Ca = 0.05$, $\lambda = 10$; $\Delta t^* = 5\times10^{-3}$; tube length $L_w = 10\,R$.

continuous across the drop interface, we seek $\Delta\boldsymbol{f} = \Delta f_n\,\boldsymbol{n}$. We impose

$$\oint_{\mathscr{S}} \Delta f_n\,\boldsymbol{n}\;\mathrm{d}S = \boldsymbol{0} \tag{3.4}$$

because the drop is freely suspended in the flow. The translational velocity V is unknown, and must be chosen so as to ensure

$$(\boldsymbol{u} - V\boldsymbol{e}_x)\cdot\boldsymbol{n} = 0 \tag{3.5}$$

everywhere on the drop surface.

The boundary integral problem (2.6) with unknowns $(\boldsymbol{u}, \boldsymbol{f}^w, \Delta f_n, V)$ is singular since it admits an infinity of solutions. Indeed, an arbitrary uniform pressure p_0 may be added to the stress distribution Δf_n, since

$$\oint_{\mathscr{S}} \boldsymbol{J}\cdot\boldsymbol{n}\;\mathrm{d}S = \boldsymbol{0} \quad\text{and}\quad \oint_{\mathscr{S}} \boldsymbol{n}\;\mathrm{d}S = \boldsymbol{0}. \tag{3.6}$$

Therefore, we solve the mobility problem by means of a singular decomposition of the linear system induced by (2.6), seeking the minimum norm solution (Lapack routine `DGELSS`). This procedure boils down to selecting the normal stress distribution that has a zero mean value over the drop surface. Analytic results for an asymptotically small droplet (Hetsroni, Haber & Wacholder 1970; Brenner 1971) are available in the literature and will be used in § 5 to validate this method in the limit $\alpha \ll 1$.

4. Asymptotic analysis for a long slender drop in a capillary

We consider a laminar annular flow of two liquids driven by a pressure gradient G in a capillary of radius R. The inner liquid, of viscosity $\lambda\mu$, occupies a cylinder of radius $R\delta < R$, and the outer liquid, of viscosity μ, occupies the annular film of thickness $h = (1-\delta)R$. Continuity of the fluid velocity $\boldsymbol{u}$ and of the tangential stress

across the interface yields

$$\boldsymbol{u}(\boldsymbol{x}) = \begin{cases} \dfrac{G}{4\mu}\left(r^2 - R^2\right)\boldsymbol{e}_x, & R\delta \leqslant r \leqslant R, \\ \dfrac{G}{4\lambda\mu}\{r^2 + (\lambda-1)\delta^2 R^2 - \lambda R^2\}\,\boldsymbol{e}_x, & 0 \leqslant r \leqslant R\delta. \end{cases} \tag{4.1}$$

The total volumetric flow rate through a tube section is

$$Q = 2\pi \int_0^R \boldsymbol{u}\cdot\boldsymbol{e}_x\, r\,\mathrm{d}r = -\frac{\pi G R^4}{8\mu}\{1 + (\lambda^{-1} - 1)\delta^4\}, \tag{4.2}$$

and if we define the mean velocity U such that $Q = \pi R^2 U$, the pressure gradient is

$$G = -\frac{8\mu U}{R^2}\{1 + (\lambda^{-1} - 1)\delta^4\}^{-1}. \tag{4.3}$$

If the inner cylinder represents a long, but finite drop moving with velocity V, then

$$\pi(R\delta)^2 V = 2\pi \int_0^{R\delta} \boldsymbol{u}\cdot\boldsymbol{e}_x\, r\,\mathrm{d}r = \frac{\pi G R^4}{8\mu}\left(2\delta^4 - 2\delta^2 - \delta^4\lambda^{-1}\right), \tag{4.4}$$

so that

$$\frac{V}{U} = -\frac{GR^2}{8\mu U}\left\{2 + (\lambda^{-1} - 2)\,\delta^2\right\} = \frac{2\lambda + (1-2\lambda)\,\delta^2}{\lambda + (1-\lambda)\,\delta^4}. \tag{4.5}$$

Equation (4.5) reveals that elongated drops with $\lambda < 1/2$ may travel faster than $2U$, the maximum velocity of the suspending fluid, whereas $V \leqslant 2U$ otherwise.

When the capillary number is small, the drop fills the width of the tube, and hydrodynamic interactions with the wall play an important role in determining the deformation of the drop. As Ca increases, viscous forces increase and the drop deforms further, becoming longer and thinner, with its surface closer to the centreline of the capillary and farther from the wall. Capillary forces increase as the drop becomes thinner, and we now examine whether the diameter of the cylindrical drop can be controlled by the balance between capillary and viscous forces at the front end of the drop. For thin slender drops ($\delta \ll 1$), the velocity of the drop relative to the unperturbed velocity $2U$ along the centreline is, by (4.5),

$$V - 2U = -\delta^2(2 - \lambda^{-1})U - 2\delta^4(\lambda^{-1} - 1)U + O(\delta^6 U). \tag{4.6}$$

This relative velocity, acting on an approximately hemispherical end cap, produces stresses of order $\mu(2U - V)/(R\delta)$ on the surface of the drop. However, we expect these to be balanced by hydrodynamic stresses within the drop, without causing deformation, as found by Hetsroni *et al.* (1970) for a small spherical drop on the centreline of Poiseuille flow. Hetsroni *et al.* showed that deformation was caused by flow perturbations due to the presence of both the wall and the drop. Disturbances to Stokes flow in a capillary of radius R decay exponentially over a length scale $O(R)$ (Liron & Shahar 1978), and the viscous stress perturbation at the front and rear of the drop due to the presence of the walls is of order $\mu(2U - V)/R$. The external shear stresses on the surface of the drop are balanced by internal shear stresses, with corresponding internal velocity perturbations of order $\delta(2U - V)/(1+\lambda)$: perturbed normal stresses within the drop are therefore of order $\lambda\mu(2U - V)/[(1+\lambda)R]$. The sign of the hydrodynamic normal stress balance is not given by these arguments, but $V \leqslant 2U$ if $\lambda \geqslant 1/2$, by (4.5), and velocities at the front of the drop, shown in figure 3(*b*), are such as to tend to stretch the drop and reduce δ. A balance between

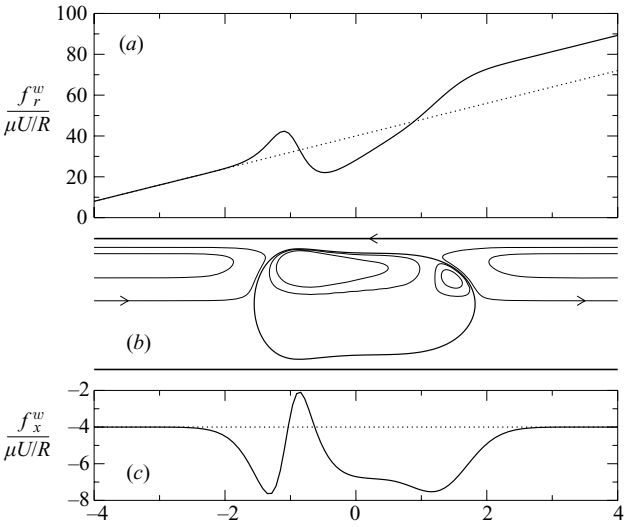

FIGURE 3. (*a*) Normal stress distribution $f_r^w = -p$ at the wall; (*b*) steady drop profile and streamlines (in the reference frame moving with the drop); (*c*) wall shear stress f_x^w; $\alpha = 1.1$, $Ca = 0.05$, $\lambda = 10$. Dotted lines: single-phase (Poiseuille) solution. The common x-axis is the dimensionless length x/R along the capillary; the computational domain is $|x| \leqslant 5R$.

normal viscous stresses and capillary forces of order $\gamma/R\delta$ becomes possible if

$$\mu \frac{2U - V}{R} \sim \frac{\gamma}{R\delta}, \quad \lambda \geqslant 1/2, \tag{4.7}$$

and we shall see in § 5.2, by comparison with full numerical computations, that the sign in (4.7) is correct. Hence, using (4.6),

$$\delta \sim (2 - \lambda^{-1})^{-1/3} Ca^{-1/3}, \quad \lambda > 1/2. \tag{4.8}$$

This suggests that very viscous drops will be slimmer than less viscous drops. The analysis leading to (4.8) requires the first term on the right-hand side of (4.6) to dominate the second term, i.e. $2 - \lambda^{-1} \gg Ca^{-2/5}$. If $\lambda = 1/2$, the first term on the right-hand side of (4.6) vanishes, and the stress balance over the front end of the drop leads to

$$\delta \sim Ca^{-1/5}, \quad \lambda = 1/2, \tag{4.9}$$

rather than (4.8). If $\lambda < 1/2$, the sign of the hydrodynamic normal stress term in (4.7) is such that the stress balance (4.7) fails: we shall see in § 5 that at sufficiently high capillary numbers, a low-viscosity drop translates at a velocity V greater than the unperturbed velocity $2U$ on the centreline of the capillary. Streamlines near the front of the drop are then quite different from those in figure 3(*b*). Moreover, numerical results (§ 5.2) show that if $\lambda < 1/2$ the radius of the cylindrical drop tends to a non-zero limit δ_∞. The gap between the drop and the capillary wall does not become large compared with the drop radius, and the deformation of the drop is not controlled solely by normal stresses at the front of the drop along the axis of the capillary. Nevertheless, we shall see in § 5.2 that when $\lambda < 1/2$ the film thickness h at the wall is close to that predicted when an infinitely long finger (rather than a drop) of viscosity $\lambda\mu$ enters the capillary. Such a finger has no rear end, suggesting that the front of the finger or drop controls the film thickness h for all λ.

Inserting (4.8) and (4.9) into (4.6), we find that the drop velocity at high Ca takes the form

$$V^* - 2 \sim -(2-\lambda^{-1})^{1/3}\, Ca^{-2/3}, \quad \lambda > 1/2; \tag{4.10a}$$

$$\sim -Ca^{-4/5}, \quad \lambda = 1/2. \tag{4.10b}$$

If the drop shape is approximated by a cylinder with two hemi-spherical caps of radius $R\delta$, the length l of the cylindrical part is given by

$$\frac{l}{R} \approx \frac{4}{3}(\alpha^3 - \delta^3)\,\delta^{-2}. \tag{4.11}$$

The pressure gradient in the absence of any drop is $G_0 = -8\mu U/R^2$, and so the increase Δp_a in pressure caused by the cylindrical part is

$$\frac{\Delta p_a^{(cyl)}}{\mu U/R} \approx \frac{(G_0 - G)\,l}{\mu U/R} \approx -\frac{32}{3}\,\frac{(1-\lambda)\,\delta^2}{\lambda + (1-\lambda)\,\delta^4}\,(\alpha^3 - \delta^3). \tag{4.12}$$

The contribution to the pressure drop of the end caps when $\delta \ll 1$ is comparable to that caused by a spherical drop of radius $a = R\delta$. Brenner (1971) found that the pressure drop due to a small, force-free spherical drop of radius $a = \alpha R$ is

$$\frac{\Delta p_a}{\mu U/R} = \frac{16}{27}\,\frac{(2+9\lambda)^2 - 40}{(1+\lambda)(2+3\lambda)}\,\alpha^5 + O(\alpha^{10}), \tag{4.13}$$

which suggests an end-cap correction

$$\frac{\Delta p_a^{(cap)}}{\mu U/R} \sim \delta^5. \tag{4.14}$$

When $\delta \ll 1$, this correction appears to be *a priori* much smaller than the contribution (4.12), unless λ is very close to 1. Therefore, according to (4.8), we find that the change in pressure caused by the presence of the drop, in the limit $Ca \gg 1$, is given by

$$\frac{R}{\mu U}\,\Delta p_a \sim \alpha^3\,(1-\lambda^{-1})(2-\lambda^{-1})^{-2/3}\,Ca^{-2/3} \quad \text{for} \quad \lambda > 1/2. \tag{4.15}$$

This leading-order increase in the pressure vanishes if $\lambda = 1$, which is expected since the contribution of the annular flow to Δp_a vanishes, as seen in (4.12). In this case, the additional pressure drop is solely due to viscous stresses at the end caps. Hence, combining (4.14) and (4.8), we obtain

$$\frac{R}{\mu U}\,\Delta p_a \sim Ca^{-5/3} \quad \text{for} \quad \lambda = 1. \tag{4.16}$$

When $\lambda = 1/2$ and $Ca \gg 1$ the drop radius δ is given by (4.9), rather than by (4.8), and so (4.12) predicts that the change in pressure is

$$\frac{R}{\mu U}\,\Delta p_a \sim -\alpha^3\,Ca^{-2/5} \quad \text{for} \quad \lambda = 1/2. \tag{4.17}$$

5. Arbitrary drop size

We now investigate numerically the effect of the parameters α, Ca and λ on the drop deformation, its translational velocity and the additional pressure drop. The influence of the viscosity contrast is investigated by comparing the results obtained for three values of λ. We choose $\lambda = 0.1$ and 10 to address the cases of low- and

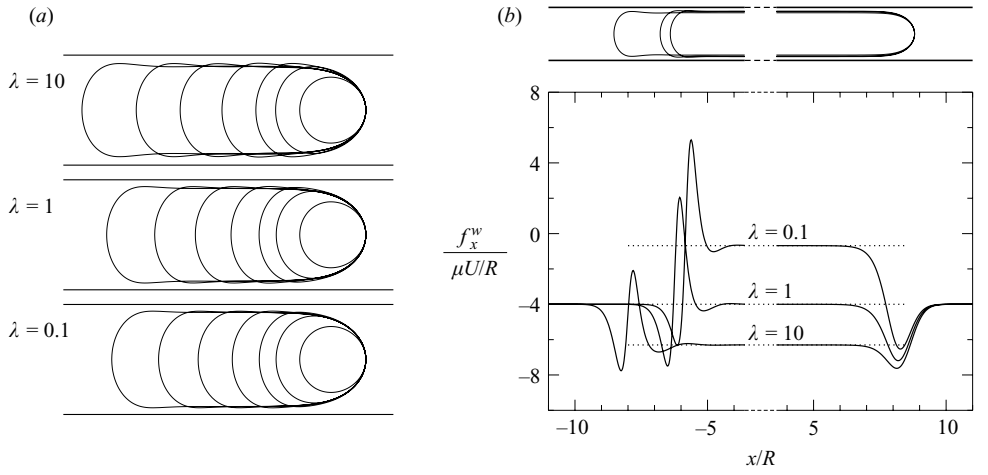

FIGURE 4. Effect of drop volume on the steady drop profile for $Ca = 0.05$, $\lambda = 0.1, 1, 10$; (*a*) moderate drop sizes, $\alpha = 0.6, 0.8, [0.1], 1.3$; (*b*) steady drop profile and wall shear stress, $\alpha = 2$; dotted, wall shear stress in the film region calculated from V using (4.5) and (5.1).

high-viscosity drops, respectively, and $\lambda = 1$ to highlight the effect of size and capillarity, independently of viscous effects.

We show in figure 3 the typical result of a simulation, i.e. the steady drop shape and the wall stress for set values of λ, α and Ca. The streamlines reveal the typical flow patterns inside and outside the drop in the reference frame moving with the drop at constant velocity. Note that in this reference frame, the capillary wall moves at constant velocity $-V$, i.e. from right to left in figure 3(*b*).

The inner flow consists of three recirculation zones revealing the existence of two stagnation rings on the surface, in addition to the two stagnation points on the axis imposed by the axisymmetry of the flow. These vortices are due to the motion of the drop along the capillary at a velocity larger than the mean flow velocity U, as will be shown later in further detail. Figure 3 only shows two recirculation eddies inside the drop; the third one is located at the rear of the drop, but could not be drawn owing to the very small velocity of the inner fluid in this region.

The analysis of the viscous stress at the wall indicates that the perturbation due to the presence of the drop rapidly vanishes up- and downstream, as the stress reduces to that of a single-phase pressure-driven flow (uniform pressure gradient $-8\mu U/R^2$ and wall shear stress $-4\mu U/R$). This validates the hypothesis of undisturbed flow sufficiently far from the drop made in § 2. The normal stress $f_r^w = -p$ at the wall, and so it is straightforward to use f_r^w away from the drop (where the pressure is uniform over the tube cross-section) to calculate the additional pressure difference Δp_a needed to maintain a flow rate $\pi R^2 U$ when the drop is present in the capillary.

5.1. *Effect of drop size*

Figure 4 shows the steady drop shape and the wall shear stress for different drop volumes at $Ca = 0.05$, and for three different viscosity ratios ($\lambda = 0.1, 1, 10$). In all cases, the deformed shape is asymmetric: since the drop is placed in a pressure gradient, the curvature at the front is higher than that at the rear. This is a general feature of deformable drops flowing in tubes (Martinez & Udell 1990). For a given capillary number, the drop deformation is small and depends little on λ when the drop is sufficiently small (e.g. $\alpha \leqslant 0.6$ for $Ca = 0.05$ in figure 4*a*). Size effects become clearly visible in figure 4(*a*) for $\alpha \geqslant 0.9$ owing to the increased drop deformability

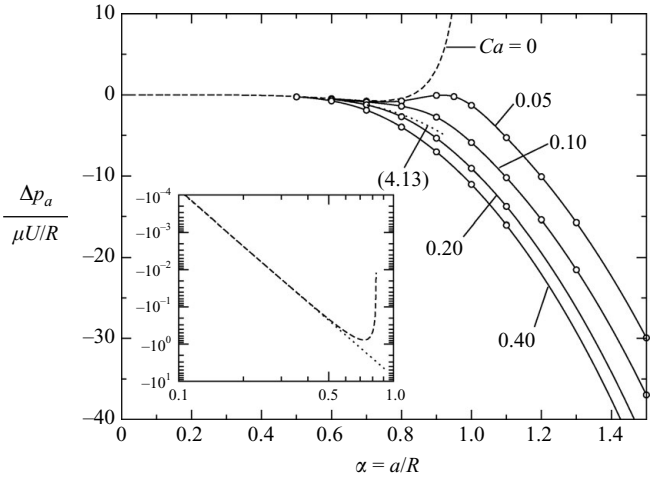

FIGURE 5. Effect of drop size on the additional pressure drop for $\lambda = 0.1$ and different capillary numbers. The dotted line shows the analytic prediction (4.13) of Brenner (1971) for a small spherical droplet. Inset: (4.13) and $Ca = 0$ in logarithmic scaling.

and the presence of the wall. Overall, an asymptotic situation is reached for $\alpha > 1.1$, approximately, where the front and rear of the drop are unchanged and where an increase in drop volume merely lengthens the drop (Ho & Leal 1975; Martinez & Udell 1990). When the drop is sufficiently large, a uniform viscous film appears between the drop and the wall. The film thickness $h = (1-\delta)R$ can be calculated from the drop velocity V using (4.5). In the film region, the wall shear stress is that of an annular flow:

$$f_x^w = -4\,\frac{\mu U}{R}\,\{1 + (\lambda^{-1} - 1)\,\delta^4\}^{-1}. \tag{5.1}$$

The dotted lines in figure 4(*b*) show, for very long drops ($\alpha = 2$), the wall stress (5.1) calculated from the drop velocity V obtained numerically. The good agreement between the wall stress (5.1) and the results of the full numerical simulations shows that the determination of h from the computed drop velocity V and (4.5) is valid. The film thickness measured from the drop profile also matches the value of h determined from V (up to four digits). The high-viscosity drops undergo a larger shear stress and therefore are more deformed than low-viscosity drops. For the same reason, the film thickness between a large drop and the wall increases with λ.

We show in figure 5 the additional pressure difference Δp_a between the extremities of the tube due to the presence of the drop as a function of the drop size, for various capillary numbers and $\lambda = 0.1$. Generally speaking, when $\lambda < 1$, part of the fluid in the tube has a lower viscosity than the suspending liquid, which makes it easier to drive the flow at a fixed flow rate. Consequently, Δp_a tends to be negative. However, capillary forces have to be overcome to deform the drop, with $\Delta p_a > 0$ when Ca is small. At intermediate capillary numbers, the competition between these two effects may lead to a non-monotonic variation and a local maximum value of Δp_a^* as the drop size varies. In the limit case of a spherical drop ($Ca = 0$), the capillary forces are infinitely greater than the viscous forces, and the (non-dimensional) additional pressure tends to infinity as the drop size approaches that of the tube ($\alpha \to 1$).

In the absence of viscosity contrast ($\lambda = 1$, figure 6*b*), only capillarity matters. In this case, the disturbance on the pressure field is exclusively due to the front and

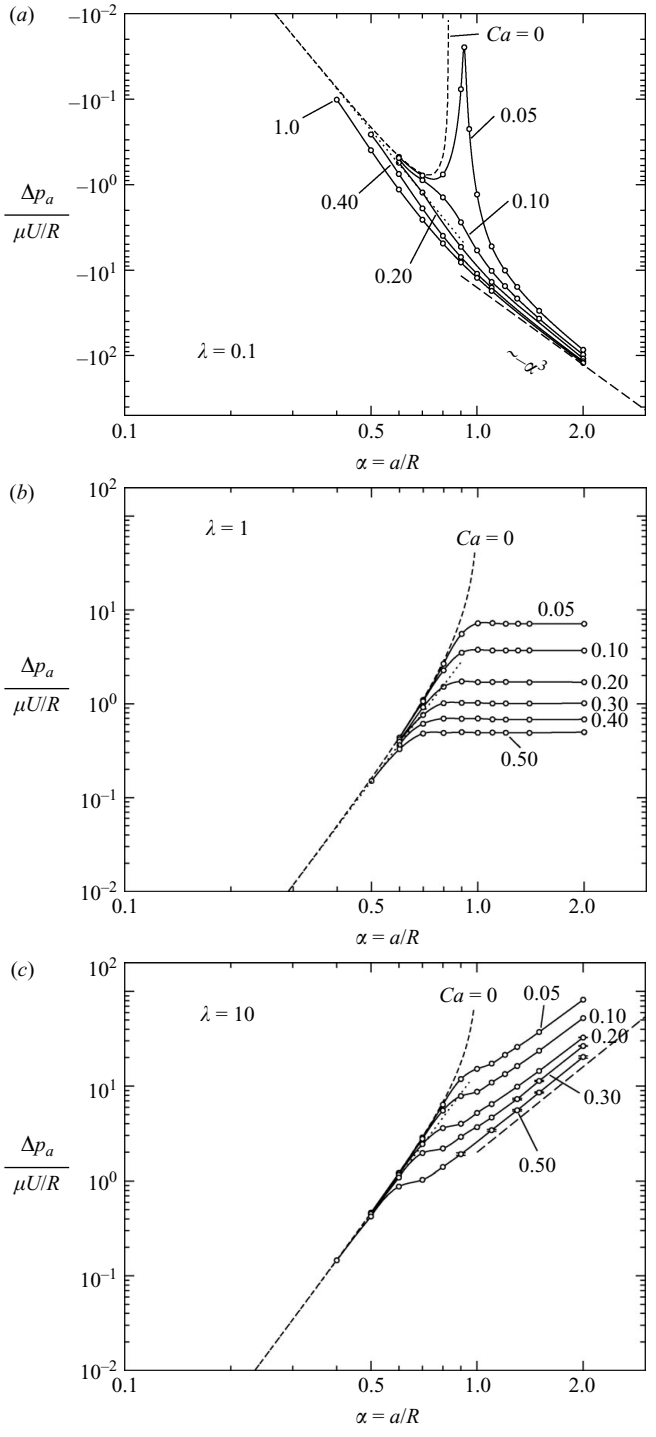

FIGURE 6. Same as figure 5 in logarithmic scaling and for three values of λ. Thick dashed lines, $\sim \pm\alpha^3$.

rear of the drop, and the effect of an asymptotic drop shape is clearly marked by the appearance of a plateau value of Δp_a^* as the drop size increases. This plateau value depends upon Ca since the additional pressure drop is solely due to capillary effects.

For high-viscosity drops, both capillarity and viscosity contrast contribute to increase the pressure drop (see figure 6c for $\lambda = 10$). As will be discussed in § 6, a capillary instability develops for high-viscosity drops above a critical Ca, and the drops enter an oscillatory regime. In this case, error bars in figure 6(c) (and in other figures) indicate the oscillation amplitude around the mean value (e.g. $\alpha \geqslant 0.9$ for $Ca = 0.5$ in figure 6c), though the error bars are generally smaller than the plotted symbols.

Figure 6 shows that up to $a = 0.5\,R$, typically, our numerical results for spherical drops ($Ca = 0$) are in good agreement with the result (4.13) of Brenner (1971) for asymptotically small drops. The numerical results for deformable drops ($Ca \neq 0$) depart from those obtained for $Ca = 0$ as both α and Ca increase, since these two parameters determine the drop deformability.

The drop translational velocity V is shown in figure 7 as a function of α for different capillary numbers and two values of λ. For a vanishingly small droplet moving along the centreline of a capillary, Hetsroni *et al.* (1970) give

$$V^* = \frac{V}{U} = 2 - \frac{4\lambda}{2 + 3\lambda}\,\alpha^2 + O(\alpha^3). \tag{5.2}$$

As $\alpha \to 0$, the drop velocity V approaches the unperturbed fluid velocity $2U$ on the axis. For sufficiently large drops, a uniform film forms between the drop and the wall. The film thickness h is then determined by the balance between viscous and capillary forces at the end caps, depending solely on Ca and λ. Since the drop velocity V is given by h and λ through (4.5), the drop is expected to move at constant velocity above a certain volume. This situation is clearly visible in figure 7, where we find that the plateau value of V^* is reached for $\alpha > 1.1$, typically.

5.2. *Effect of the capillary number*

Figures 8(a) and 8(b) show, for two drop sizes, the steady shape of a high-viscosity drop ($\lambda = 10$) under an increasing flow strength. Noticeably, the drop exhibits a bulge at the rear and rapidly elongates as Ca increases. A steady state cannot be attained above a critical capillary number, owing to the appearance of a capillary instability leading to a oscillatory regime discussed in § 6. The most deformed profiles in figures 8(a) and 8(b) correspond to the highest capillary number for which we could identify a steady state.

When λ is reduced to 0.1 (figure 8c, d), the drop no longer exhibits a rear bulge above a certain capillary number (e.g. $Ca \geqslant 0.5$ in figure 8d), and ultimately shows a tendency to dimple at the rear. As observed in § 5.1, a low-viscosity drop is clearly less deformed than a high-viscosity drop at a given capillary number (figure 4a). Above a critical capillary number, the rear dimple turns into a jet as surface tension is no longer able to balance viscous stresses. This phenomenon, observed experimentally (e.g. Olbricht & Kung 1992), is described in § 6.

The effect of Ca on the drop velocity V and the additional pressure drop Δp_a is illustrated in figures 9–14. As Ca increases, the drop becomes more elongated and its surface is farther from the capillary wall: it therefore moves faster. We recall that when $\alpha < 1$ the undeformed drop fits in the capillary and the hydrodynamic problem admits a solution for $Ca = 0$ (§ 3.2). However, this solution is off to the left of the logarithmic scale, which explains the peculiar aspect of the plots in figures 9(a) and

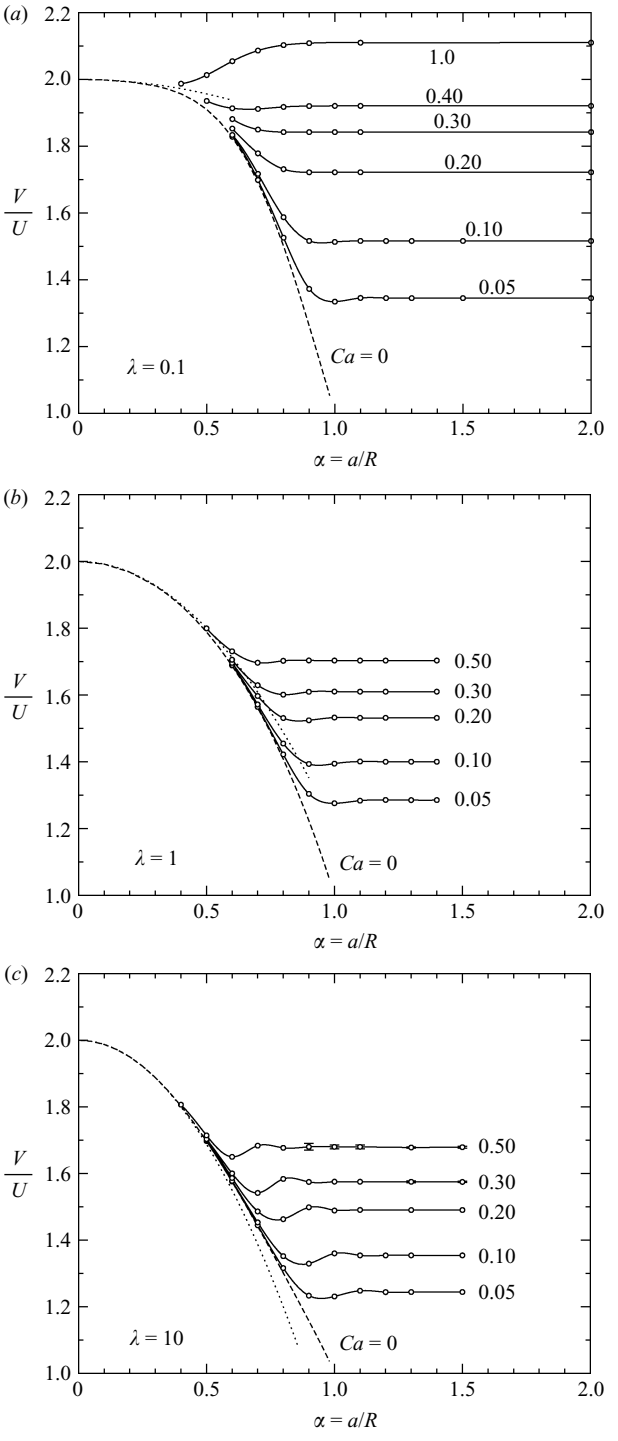

FIGURE 7. Drop translational velocity V as a function of α for different capillary numbers and three values of λ. Dotted lines: asymptotic prediction (5.2) of Hetsroni *et al.* (1970) for $\alpha \ll 1$.

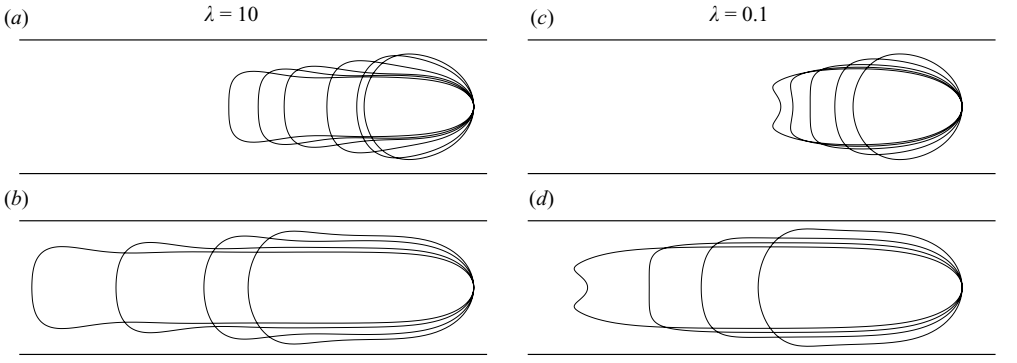

FIGURE 8. Steady drop profile at increasing capillary number; (*a*) $\lambda = 10$, $\alpha = 0.8$, $Ca = 0.05, 0.1, [0.1], 0.5$; (*b*) $\lambda = 10$, $\alpha = 1.1$, $Ca = 0.05, 0.1, 0.2, 0.3$; (*c*) $\lambda = 0.1$, $\alpha = 0.8$, $Ca = 0.05, 0.2, 0.5, 1, 2$; (*d*) $\lambda = 0.1$, $\alpha = 1.1$, $Ca = 0.05, 0.2, 0.5, 2.35$.

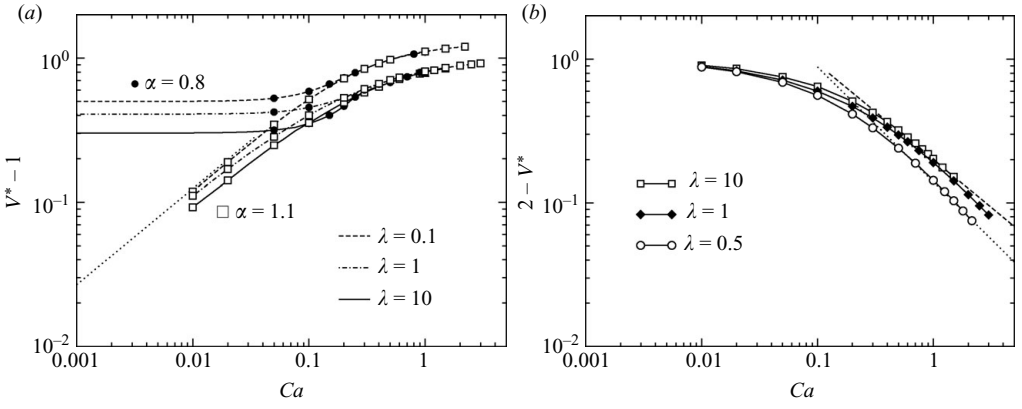

FIGURE 9. Dimensionless velocity $V^* = V/U$ *vs.* Ca for $\lambda = 0.1, 1, 10$ and different drop sizes: ●, $\alpha = 0.8$; □, $\alpha = 1.1$. The dotted line shows the velocity of a Bretherton bubble, $V^* \approx 1 + 1.29\,(3\,Ca)^{2/3}$; (*b*) same as (*a*), but showing how V approaches the axis velocity $2U$ as Ca increases, for $\alpha = 1.1$ and $\lambda \geqslant 0.5$; dashed, $\sim Ca^{-2/3}$; dotted, $\sim Ca^{-4/5}$.

12 for $\alpha = 0.8$, where we have interpolated the plotted quantity between $Ca = 0$ and the first non-zero Ca computed numerically.

In figure 9, we plot $V - U$ *vs.* Ca to illustrate how much the drop velocity exceeds the average velocity of the suspending fluid. For drops fitting undeformed in the capillary ($\alpha < 1$), the finite value of $V^* = V/U$ obtained for $Ca = 0$ decreases as λ increases owing to the increasing drag induced by the wall. We also note that $(\partial V^*/\partial Ca)_{Ca=0} = 0$, which means that when $\alpha < 1$, V^* increases only slowly with Ca (up to $Ca \sim 10^{-2}$, typically). If $\alpha \geqslant 1$, the drop cannot flow in the capillary without deforming. For long inviscid bubbles ($\lambda = 0$), Bretherton (1961) showed that as $Ca \to 0$, the drop velocity approaches the mean velocity of the outer flow according to $V^* \approx 1 + 1.29\,(3\,Ca)^{2/3}$. Note that in the limit $Ca \ll 1$, our capillary number, based on U, is the same as Bretherton's, based on the bubble velocity V. We observe in figure 9 that our results approach Bretherton's asymptote as λ decreases. Moreover, as shown by Hodges *et al.* (2004), we see that $V^* - 1 \sim Ca^{2/3}$ as $Ca \to 0$ for all values of λ, where the multiplying factor is a decreasing function of λ (viscous drops are always slower than an inviscid

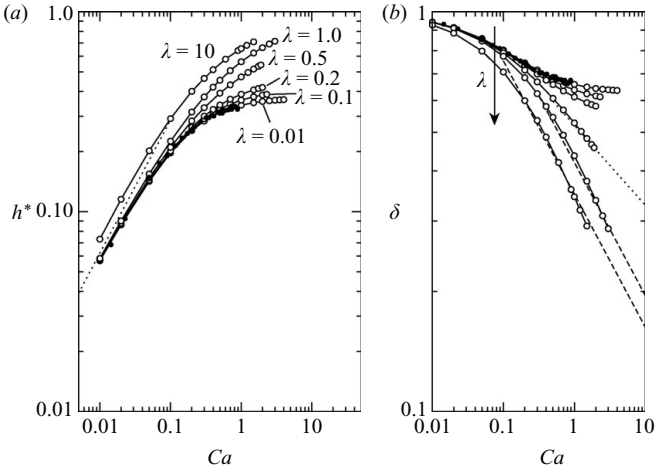

FIGURE 10. (*a*) Film thickness $h^* = h/R$ *vs. Ca* for long drops and different values of λ; dotted, the Bretherton bubble, $h^* \approx 1.3375\,Ca^{2/3}$; (*b*) drop breadth $\delta = 1 - h^*$ *vs. Ca* for the same values of λ as in (*a*); dashed, $\sim Ca^{-1/3}$; dotted, $\sim Ca^{-1/5}$; ●, experimental results of Taylor (1961).

bubble owing to the shear stress in the viscous film between the drop and the capillary wall).

At high capillary numbers, the velocity of the drop exceeds the axis velocity $2U$ for $\lambda = 0.1$ (figure 9*a*), as predicted in (4.5) for $\lambda < 0.5$. This was also observed in our simulations for $\lambda = 0.01$, 0.05 and 0.2, although these results are not shown in figure 9(*a*) for clarity. For sufficiently viscous drops ($\lambda \geqslant 0.5$), on the other hand, V approaches $2U$ from below as Ca increases; the balance between viscous and capillary forces at the drop tips leads to $2 - V^* \sim Ca^{-4/5}$ for $\lambda = 0.5$ and $\sim Ca^{-2/3}$ for $\lambda > 0.5$, (4.10), as observed numerically for $\lambda = 0.5$ and $\lambda = 10$ (figure 9*b*). When $\lambda = 1$, however, the agreement with (4.10) is somewhat poorer.

Figure 10 shows the evolution of the dimensionless drop breadth δ and film thickness $h^* = 1 - \delta$ as Ca increases, for long drops and a wide range of viscosity ratios. Figure 10(*b*) clearly shows the difference between low-viscosity drops ($\lambda < 0.5$), high-viscosity drops ($\lambda > 0.5$) and the special case $\lambda = 0.5$. For $0 < \lambda < 0.5$, our numerical results suggest that the film thickness h^* is bounded above by a limit $1 - \delta_\infty$ corresponding to

$$\delta_\infty^2 = \frac{2}{5}\,\frac{1-2\lambda}{1-\lambda} \quad \text{i.e.} \quad \frac{V_\infty}{U} = \frac{50\,\lambda(1-\lambda) + 10\,(1-2\lambda)^2}{25\,\lambda(1-\lambda) + 4\,(1-2\lambda)^2}, \quad \lambda < 1/2. \tag{5.3}$$

We find that both $\delta - \delta_\infty$ and $V_\infty^* - V^*$ ultimately decay as Ca^{-1}, approximately. Figure 11 shows the velocity $V(\delta)$ predicted by the annular flow analysis (4.5), together with the upper bound (5.3), for various values of λ. The limit $h/R \to 0$ corresponds to $Ca \to 0$, for which $V^* = V/U \to 1$ for any value of λ (Hodges *et al.* 2004). When Ca is sufficiently large and the drop sufficiently long, we expect the cylindrical radius δ to be determined by flow at the front of the drop. The thickness h of the cylindrical film around the drop should therefore be similar to that of the wall film left behind during displacement of one fluid by another in a capillary. In experiments at a viscosity ratio $\lambda \approx 2.5 \times 10^{-5}$, Cox (1962) found that as Ca becomes large, the fractional amount $m = 1 - \delta^2$ of viscous fluid left behind the drop tends to the limit 0.60, which is indeed

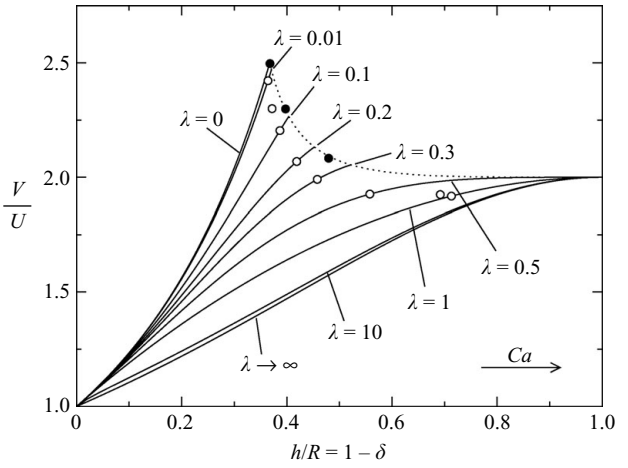

FIGURE 11. Velocity of a long drop as a function of film thickness h for various values of λ. Dotted line: approximate limit values of h and V given by (5.3) for $\lambda < 0.5$; ○, last point reached in the present work for $\lambda \leqslant 1$; ●, results of Soares *et al.* (2005) for $Ca \gg 1$ and $\lambda^{-1} = 10^3$, 12, 4.

the value given by (5.3) for $\lambda \to 0$. Soares, Carvalho & Souza Mendes (2005) used a finite-element method to compute the displacement of viscous, immiscible fluids over a wide range of capillary numbers and for viscosity ratios $10^{-3} \leqslant \lambda \leqslant 0.5$. These computations were supported by experiments at $Ca' \leqslant 0.3$, where Ca' is a capillary number based on the velocity of the tip of the invading fluid. The computed film areas $1 - \delta^2$ in their figure 11 agree well with (5.3) at $Ca' = 100$ ($40 < Ca < 50$) for $\lambda^{-1} = 10^3$, 12 and 4 (● in figure 11) and suggest the absence of a limiting film thickness when $\lambda = 0.5$, in agreement with our own results. Although our simulations show δ increasing towards δ_∞ as Ca increases, we could not approach the limit (5.3) as closely as Soares *et al.* (see ○ in figure 11) owing to drop breakup occurring at the drop rear (§ 6). This limitation does not appear in the work of Soares *et al.*, who considered the front of an infinitely long viscous finger advancing along the capillary.

Note that (5.3) implies an absolute maximal velocity of $2.5\,U$, attained by an inviscid bubble ($\lambda = 0$) at infinite capillary number. This value has also been reported by Dupont, Legendre & Fabre (2007), who studied a bubble in a capillary by experiments and volume of fluid computations, and by Martinez & Udell (1989), who performed a boundary integral analysis.

Figures 12–14 highlight the effect of the capillary number on the additional pressure drop Δp_a. Since capillary forces contribute to a rise of the pressure loss, it is natural to observe that increasing Ca decreases Δp_a^* (figure 12). At high capillary numbers, the sign of Δp_a is solely determined by λ (negative for $\lambda < 1$ and positive for $\lambda > 1$). When $\lambda = 1$, the effects of viscosity contrast vanish, so Δp_a rapidly tends to zero as soon as the viscous stresses are sufficiently high to overcome surface tension, independent of the drop volume (typically, $Ca \geqslant 0.3$). We find that Δp_a^* ultimately decays as $Ca^{-5/3}$ for $\lambda = 1$ (figure 12*b*), as predicted by (4.16). When $\lambda \neq 1$, the magnitude of the disturbance $|\Delta p_a^*|$ increases with the drop volume. The combined effects of size and viscosity contrast at high capillary numbers are clearly visible in figure 12 for $\lambda = 0.1$, 10 and $\alpha = 0.8$, 1.1, 2. For $\lambda > 1$, we find, as predicted in § 4, that Δp_a^* evolves as $Ca^{-2/3}$ at large capillary numbers (figure 12*b*). For $\lambda = 0.1$, on the other hand, Δp_a^*

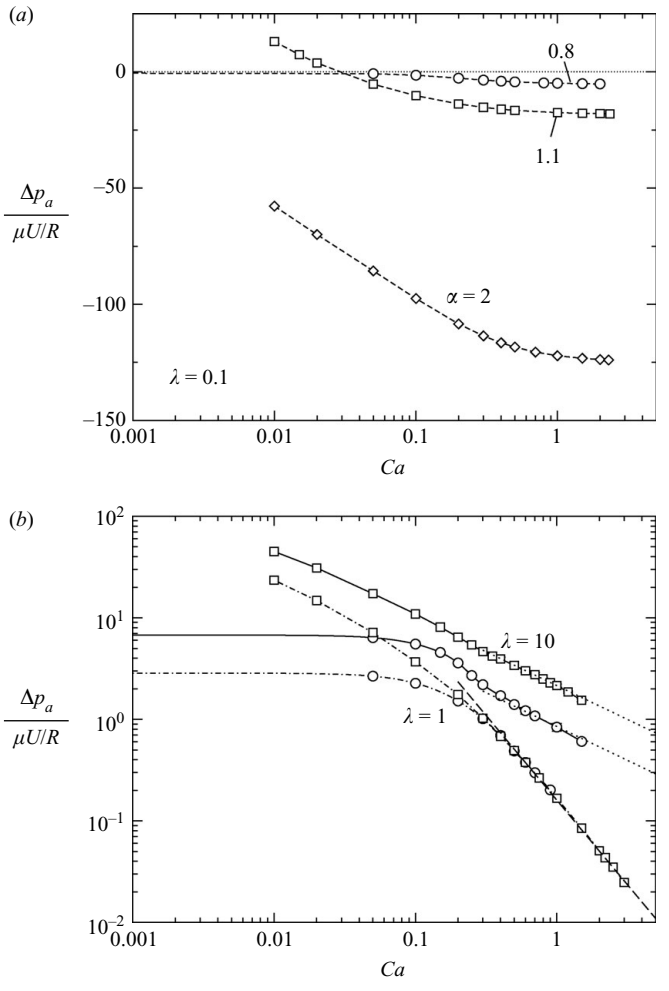

FIGURE 12. Additional pressure drop Δp_a *vs.* Ca for different drop sizes: ○, $\alpha = 0.8$; □, $\alpha = 1.1$; ◇, $\alpha = 2$; (*a*), $\lambda = 0.1$ (dashed); (*b*), $\lambda = 1, 10$ (dot-dashed, solid, resp.); dotted lines, $\sim Ca^{-2/3}$ (4.15), thick dashed line, $\sim Ca^{-5/3}$ (4.16).

seems to approach a plateau as the capillary number increases towards the maximum value for which we could find a steady solution.

In figure 13 we investigate the variation of the additional pressure drop with Ca in the case of long, low-viscosity drops ($\alpha = 2$, $\lambda < 1$). When $\lambda = 0.5$, we find that at high Ca and for two drop volumes ($\alpha = 1.1, 2$), Δp_a^* evolves as $-Ca^{-2/5}$, as predicted by (4.17). However, the analysis of § 4 fails when $\lambda < 0.5$, and we see in figure 13 that Δp_a is not decreasing towards zero at the highest capillary numbers for which the numerical computations found a steady drop shape. Also shown in figure 13 are the predictions of Bretherton (1961) and Ratulowski & Chang (1989) for long inviscid bubbles ($\lambda = 0$) at vanishingly small capillary numbers. In Bretherton's analysis, the pressure drop $\Delta p_B^* \approx 10.026\, Ca^{-1/3}$ is that across the bubble. Since the bubble is inviscid, Δp_B is solely due to the end caps, independent of the bubble length L. With our notation, however, $\Delta p_a^* = \Delta p_B^* - 8L^*$. In figure 13, we have approximated L for a given volume by assuming a cylindrical shape with hemi-spherical caps of width

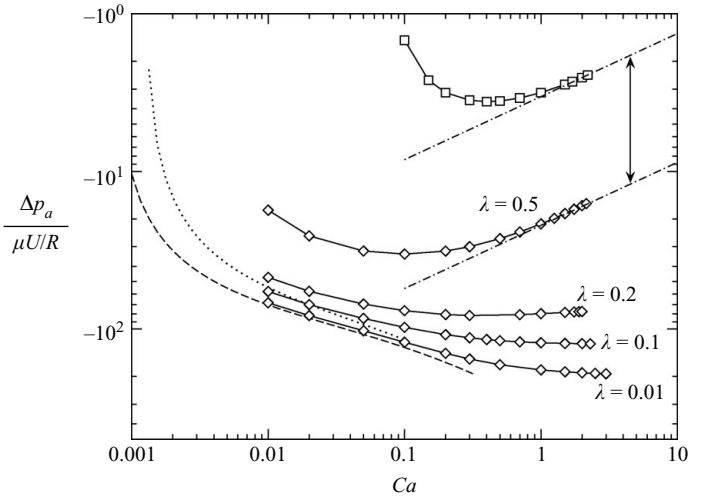

FIGURE 13. Additional pressure drop *vs.* Ca for long, low-viscosity drops ($\diamond$, $\alpha = 2$, $\lambda < 1$). Dotted: the Bretherton bubble for $\alpha = 2$; dashed: asymptotic correction of Ratulowski & Chang (1989); dot-dashed, $\sim -Ca^{-2/5}$ predicted for $\lambda = 0.5$; $\square$, $\alpha = 1.1$, $\lambda = 0.5$. The double arrow indicates a multiplying factor of $(1.1/2)^{\pm 3}$.

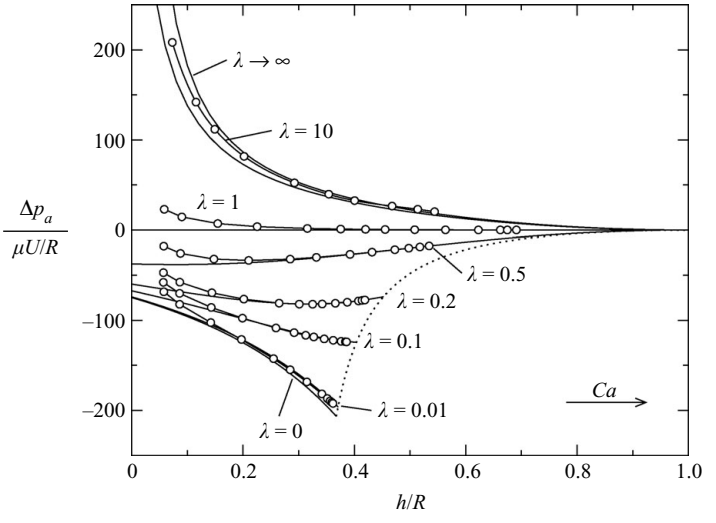

FIGURE 14. Additional pressure drop Δp_a *vs.* film thickness h for long drops ($\alpha = 2$). Thin lines: asymptotic value (4.12) when the end caps are neglected; $\circ$, numerical results. Dotted: approximate limit film thickness from (5.3) for $\lambda < 1/2$.

$R - h$, where $h \approx 1.3375\, R\, Ca^{2/3}$ is the film thickness predicted by Bretherton as $Ca \to 0$. Similarly for Ratulowski & Chang (1989), with $\Delta p^*_{RC} \approx \Delta p^*_B - 12.6\, Ca^{-0.05}$, we observe that our numerical results approach these predictions for $(\lambda, Ca) \ll 1$.

Figure 14 compares our numerical results with the annular flow predictions of § 4 by showing the evolution of Δp_a as a function of the film thickness h between the tube wall and a very long drop ($\alpha = 2$). The film thickness has been calculated from the drop velocity V through (4.5). For $\lambda < 0.5$, our numerical results indicate that the dimensionless film thickness and additional pressure drop change very slowly as the

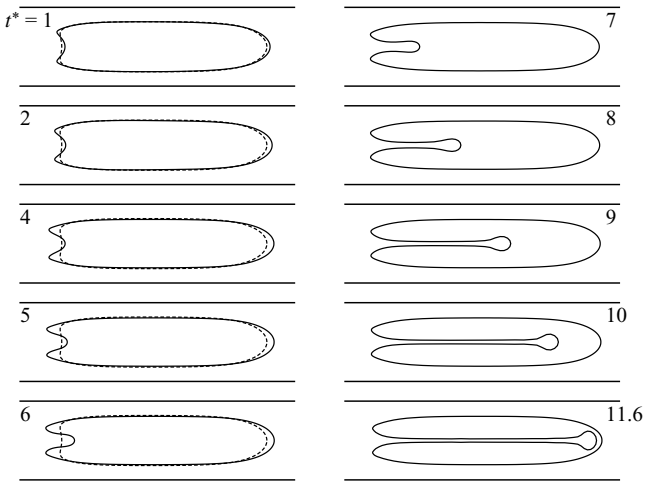

FIGURE 15. Re-entrant jet for a low-viscosity drop; $\lambda = 0.1$, $\alpha = 1.1$; Ca is increased from 1 to 2 at $t = t_0 = 0$; dashed line: steady drop profile at $Ca = 1$.

capillary number increases towards the highest value for which a steady state was obtained. This suggests the existence of limit points along the corresponding curves in figure 14, and we show our conjecture (5.3) as a dotted line.

In figure 14, the difference between the full numerical computations and the curves derived from the annular flow model of § 4 allows us to estimate the total contribution of the two end caps to the additional pressure drop Δp_a. At all viscosity ratios, we find (as expected) that the difference between our numerical results and (4.12) decreases as Ca increases, since (*a*) the drop elongates, and (*b*) the capillary effects of the end-caps decrease, by definition of Ca. Even when the viscosity ratio is small, the annular flow model predicts the pressure drop surprisingly well at sufficiently high capillary numbers (i.e. when h/R is sufficiently large in figure 14). At lower capillary numbers, when the film thickness is small, the annular flow model still gives good predictions when λ is large since the pressure gradient (4.3) in the viscous film increases with λ, and the total pressure drop is more likely to be dominated by that in the film around a sufficiently long drop (e.g. $\lambda = 10$ in figure 14). Conversely, as $\lambda \to 0$, the fluid in the film is at rest, and Δp_a is solely determined by the end caps (Bretherton 1961). Therefore, when $\lambda \ll 1$ and $h/R \ll 1$ the approximation (4.12) holds only for extremely long drops.

6. Oscillatory motion and drop breakup

We were unable to find steady drop shapes above a critical value of the capillary number. The critical capillary number Ca_c depends upon the drop size and the viscosity ratio, and the post-critical drop behaviour depends upon the viscosity ratio. For low viscosity ratios ($\lambda < 1$), the drop breaks up owing to the appearance of a re-entrant jet at the rear (figure 15). The jet develops when the normal stress balance is no longer achieved by surface tension. This phenomenon was observed experimentally by Goldsmith & Mason (1963) and Olbricht & Kung (1992). It has also been captured numerically by Tsai & Miksis (1994) from initially spherical or ellipsoidal drop shapes. Note that the appearance of a re-entrant jet at a given capillary number does not necessarily mean that no steady state exists for this value of Ca. Indeed, the instability

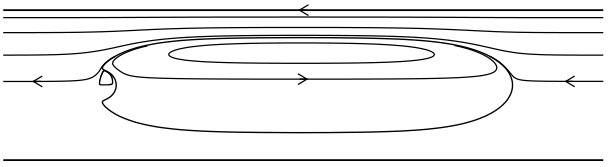

FIGURE 16. Flow pattern for $\lambda = 0.01$, $\alpha = 1.1$, $Ca = 3.5$. Note that $V > 2U$.

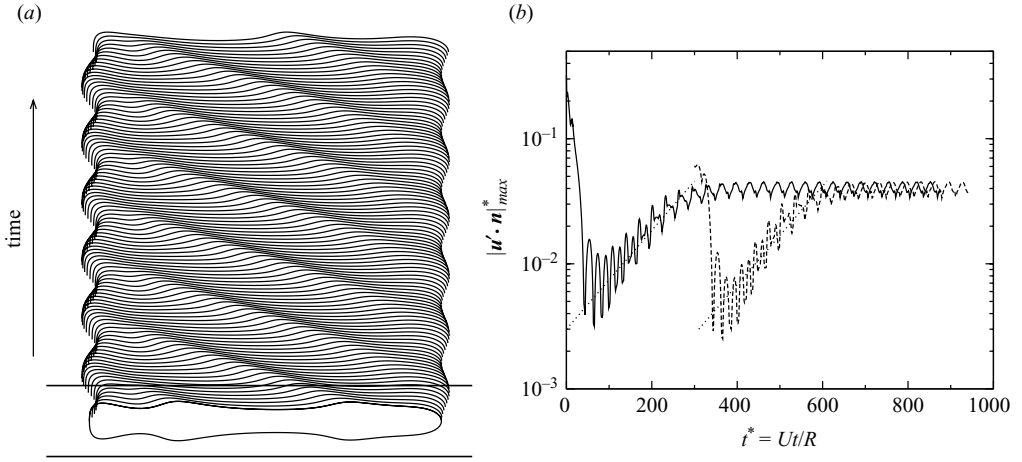

FIGURE 17. (*a*) Travelling wave instability for a high-viscosity drop in the reference frame of the drop centre of mass; $\lambda = 10$, $\alpha = 1.1$, $Ca = 0.5$. The capillary wall is shown for the first (bottom) profile. The dimensionless period of the motion is approximately 32.5. (*b*) For the same (λ, α, Ca), time evolution of the maximum normal velocity $|\boldsymbol{u}' \cdot \boldsymbol{n}|_{max}$ on the drop surface, where $\boldsymbol{u}' = \boldsymbol{u} - \boldsymbol{V}$; solid line: $N = 100$, $\Delta t^* = 0.005$; dashed: simulation restarted from the steady state obtained for $Ca = 0.3$, $N = 160$, $\Delta t^* = 0.002$; dotted: $\sim e^{t/\tau}$ with $\tau^* = 110$.

shown in figure 15 develops when Ca is increased from 1 to 2, but is not observed if Ca is increased from 1.9 to 2. This initial drop shape dependence of transient Stokes flows after a significant step change in capillary number is well known (e.g. Stone & Leal 1989). Finding the critical value Ca_c requires a gradual increase of Ca by small steps until no steady state can be attained. For example, for $\lambda = 0.1$, $\alpha = 1.1$ (as in figure 8*d*), we identified a critical capillary number slightly above $Ca = 2.35$ (the last value for which a steady state could be found); increasing Ca from 2.35 to 2.40 led to a jet. The values of Ca_c reported below are mean values between the last stable and the first unstable capillary numbers. The flow field in this case (figure 16) can be likened to that around a confined Rankine ovoid formed by a source of strength $Q_s = \pi R^2 U(1-\lambda)\,\delta^4/[\lambda + (1-\lambda)\delta^4]$ near the front of the drop, together with an equal and opposite sink near the rear of the drop, added to the unperturbed Poiseuille flow. The sink at the rear of the drop ultimately causes instability due to an inward-pointing jet of the exterior fluid.

For high viscosity ratios, the drop becomes very stretched as Ca increases, up to the point where a capillary instability develops (figure 17*a*). The drop does not break up, owing to its motion along the tube, and a travelling wave sets in and runs through the drop from front to rear. These capillary waves resemble the inertia- and gravity-driven waves seen by Bai, Chen & Joseph (1992) in an experimental study of vertical two-phase pipeline flows. For the same parameters as in figure 17(*a*) ($\lambda = 10$,

$\alpha = 1.1$, $Ca = 0.5$), figure 17(*b*) shows the time evolution of the maximum normal velocity along the drop profile in the reference frame moving with the drop centre of mass. We recall that in this reference frame, a steady drop appears fixed, because the normal velocity $u'_n = \boldsymbol{u}' \cdot \boldsymbol{n}$ vanishes everywhere on the drop surface. We observe that the drop initially evolves towards what we might expect to be a steady shape, and $|u'_n|^*_{max}$ decreases. The appearance of the instability is clearly visible soon after the drop has reached an almost steady shape, around $t^* = 50$, when $|u'_n|^*_{max} \sim 10^{-3}$. The perturbation exhibits an approximately exponential growth, as would predict a linear stability analysis, until it saturates as the instability gives way to the travelling capillary waves depicted in figure 17(*a*). The wave is not fore-aft symmetric: the normal velocity $|u'_n|^*$ is maximum on the leading (steeper) edge of the advancing wave(s). Generated at the front of the drop, the wave crests move towards the rear but stop growing at a distance $O(R)$ from the front. When we start the simulation from the steady state obtained for a lower capillary number (e.g. the dashed line in figure 17*b*, where *Ca* is increased from 0.3 to 0.5), we find that the drop reaches the same unsteady motion, proving that the observed behaviour is independent of the initial conditions (at least when these conditions are not too far from the final state). Figure 17(*b*) also demonstrates that the periodic motion is very well captured and sustained by the simulations over long times (the number of time steps is of order 2×10^5).

Neither the motion of the front of the drop nor that of its centre of mass is steady in a frame fixed in the capillary. The centre of mass frame used for presenting the results of figure 17 is therefore not an inertialess frame of reference. We have throughout assumed a Reynolds number $Re = \rho RU/\mu \ll 1$, but when the drop is unsteady we should also consider the time scale required for vorticity to diffuse across the drop. The ratio of the magnitude of the unsteady term $\rho\, \partial \boldsymbol{u}/\partial t$ in the Stokes equation to the viscous term is of order $\rho R^2/(T\mu) = Re\ R/(UT)$, where T is a typical time scale (the oscillation period, here). In all our simulations of oscillatory drop motion we find $TU/R > 20$, and we conclude that if $Re \ll 1$ it is appropriate to neglect the unsteady term in the Stokes equations. Note that the capillary waves appear to travel at constant velocity in the centre of mass frame, but not in the reference frame moving with the front of the drop. Although the waves are swept downstream, they nevertheless perturb the motion of the front of the drop, via both interfacial and viscous stresses.

Figure 18 shows how shape perturbations caused by a step change in capillary number either grow or are damped. For sufficiently small capillary numbers, the motion is stable, and the perturbation amplitude decreases exponentially with time. As *Ca* increases, the drop extends and the viscous film between the drop and the wall becomes thicker, allowing perturbations with larger wavelengths and amplitudes to survive; the characteristic damping time increases with *Ca*, up to the point where perturbations grow into sustained travelling waves.

Again, by gradually increasing the capillary number and starting the computation from the previous steady solution, we may seek an estimate of the critical capillary number Ca_c above which no steady solution is found. Figure 19(*a*) shows the estimated critical capillary number as a function of the drop size for $\lambda = 10$. In the absence of inertia, core-annular flows are always unstable to long wavelength capillary instabilities (Preziosi, Chen & Joseph 1989). We see from figure 19(*a*) that the finite size of the drop prevents this instability, since Ca_c increases as α decreases. The drop length L at which instability occurs increases with drop volume, and the corresponding slenderness $2R\delta/L$ of the drop decreases (figure 19*b*); the dimensionless

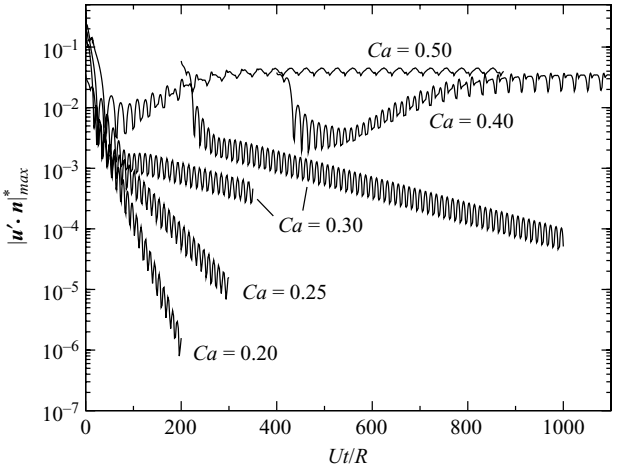

FIGURE 18. Time evolution of the maximum normal velocity for $\lambda = 10$, $\alpha = 1.1$ and different capillary numbers. The curves starting at a non-zero time correspond to simulations restarted from the steady state obtained for a lower Ca.

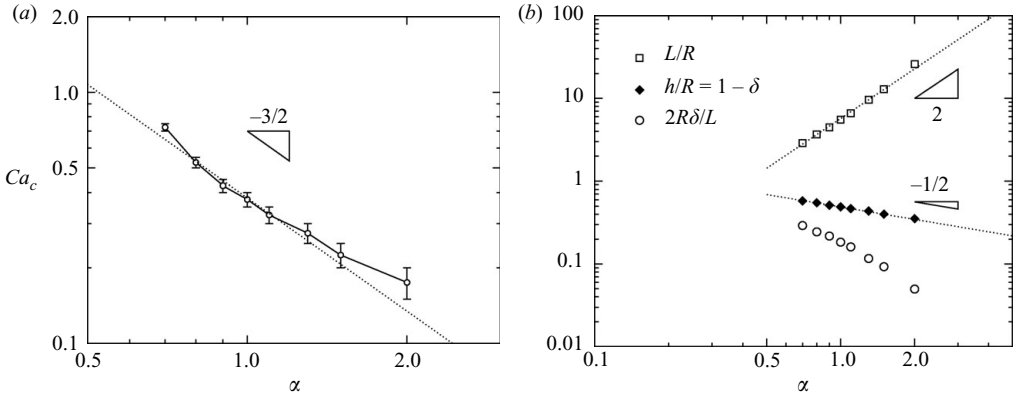

FIGURE 19. (*a*) Estimated critical capillary number Ca_c as a function of drop size for $\lambda = 10$; the error bars correspond to the last stable and the first unstable Ca; (*b*) drop length L, film thickness h and slenderness ratio $2R\delta/L$ at last stable Ca, as functions of drop size and for $\lambda = 10$. The dotted lines are inferred.

film thickness $h^* = 1 - \delta$ at which instability occurs decreases (and δ increases) as the drop volume increases. We do not at present have any explanation for these trends. The increasing drop elongation and the growing number of waves present along the drop as the flow strength increases are shown in figure 20.

Most nonlinear analyses of the instability of core-annular flow consider the effect of inertia, which can stabilize the interface when $\lambda > 1$ (Joseph & Renardy 1993). However, inertia is completely absent from the simulations presented here, and so cannot be invoked to explain the observed final steady wave amplitude. Papageorgiou, Maldarelli & Rumschitzki (1990) showed that when Reynolds numbers are small, the Kuramoto–Sivashinsky equation for wave growth includes a dispersive term which does not affect the growth of linear waves, but which can lead to nonlinear travelling waves of finite amplitude. Papageorgiou *et al.* assumed a thin annular film thickness $h^* \ll 1$. Although we find that this condition is not, in general, satisfied at the onset

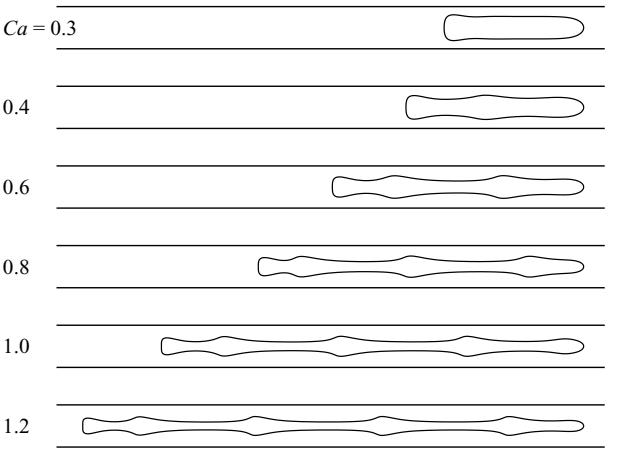

FIGURE 20. Snapshots of the drop profile for $\lambda = 10$, $\alpha = 1.1$ and various capillary numbers. Only the profile at $Ca = 0.3$ is steady.

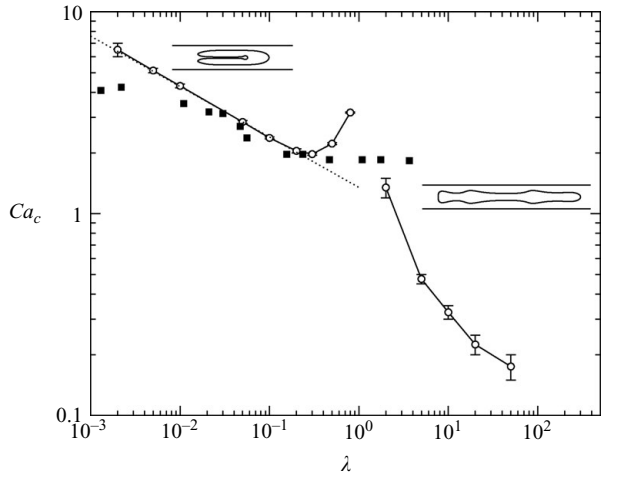

FIGURE 21. Estimated critical capillary number Ca_c as a function of viscosity ratio for $\alpha = 1.1$. The insets show the drop post-critical behaviour: re-entrant jet (low-viscosity drops) or oscillatory regime (high-viscosity drops); ■, experimental data by Olbricht & Kung (1992) for $\alpha = 1.13$. Dotted line, $\sim \lambda^{-1/4}$.

of instability (see figure 19*b*), the film between wave crests and the capillary wall is much thinner when the wave amplitude has saturated.

We summarize our results in figure 21, where we plot the critical capillary number Ca_c obtained for a wide range of viscosity ratios when $\alpha = 1.1$. For low-viscosity drops ($\lambda < 1$), the post-critical behaviour is characterized by the appearance of a re-entrant jet at the rear of the drop. Our results suggest $Ca_c \sim \lambda^{-1/4}$ for $\lambda \ll 1$. We find a quantitative agreement between our estimated Ca_c and the experimental values reported by Olbricht & Kung (1992) for this breakup mode in the range $0.01 < \lambda < 0.5$. Moreover, we find that for sufficiently large drops ($\alpha \geqslant 1.1$, typically), Ca_c is independent of the drop size for $\lambda < 1$, as observed in experiments. This is consistent with the fact that the end caps, where breakup occurs, are independent of the drop size when the drop is sufficiently long. When $\lambda > 1$, the drop enters

the oscillatory regime depicted in figure 17(*a*) as soon as Ca exceeds Ca_c. In this case, the appearance of the instability depends very much on the viscosity ratio, the dimensionless drop breadth $\delta(Ca, \lambda)$ and the dimensionless drop length $L/R \sim \alpha^3 \delta^{-2}$. For $\lambda \geqslant 0.5$, our results disagree with the experimental values shown in figure 21. This range of viscosity ratios corresponds to drops that are expected to elongate more than for $\lambda < 0.5$ as Ca increases (§ 4), but over time scales increasing with λ. Indeed, Olbricht & Kung (1992) state that 'the time scale required for appreciable drop deformation increases as λ is made larger, and this may restrict the deformation observed in most practical situations for large values of λ': as noted by Olbricht & Kung such viscous drops may reach the end of the capillary before reaching their steady/periodic state. In the example shown in figure 18 ($\alpha = 1.1$), the dimensionless time scale necessary for a fully developed periodic motion is $O(400)$, for drop velocities $V^* \approx 1.75$, which corresponds to a distance travelled of order 700 capillary radii. The largest drops studied by Olbricht & Kung corresponded to $\alpha = 1.13$, while the tube used in their experiments was 115 cm long with internal diameter 70 mm, i.e. $L_w \approx 328\, R$. According to our simulations (figures 19 and 21), the most favourable conditions for observing the oscillatory regime would be large, high-viscosity drops, allowed to move over distances much greater than the capillary diameter.

For the particular case $\lambda = 1$, we found stable shapes up to $Ca = 3$ (for $\alpha = 1.10$), corresponding to a dimensionless drop length $L/R \approx 22$ and aspect ratio $L/(2R\delta) \approx 38$. At these extreme deformations, the drop exhibits very slowly damped capillary waves near the drop tail, and reaching a steady state requires very long computations. We have identified neither a breakup nor an oscillatory regime, although the latter seems more plausible.

7. Conclusion

The boundary integral computations reported here are merely a first step towards computations of streaming potentials generated at low Hartmann number, when the electric fields are too small to modify the flow around the drop. Nonetheless, the results are of interest in their own right, and we have been able to extend previous work to a larger range of drop sizes and higher capillary numbers.

For drops sufficiently long that a uniform fluid film exists between the drop and the wall, interesting features are predicted by the annular flow analysis of § 4. The value $\lambda = 0.5$ (drop viscosity half that of the suspending liquid) plays an unexpectedly important role in determining the behaviour of the drop at high Ca. It discriminates drops that can go faster than the unperturbed centreline velocity $2U$ ($\lambda < 0.5$) if they survive to sufficiently high Ca, from those which cannot ($\lambda \geqslant 0.5$). The sign of $V - 2U$ changes significantly the flow pattern (e.g. figures 3*b* and 16). When $\lambda \geqslant 0.5$, the drop continuously thins as the flow strength increases, until breakup or unstable motion occurs. A thin drop approximation in the limit $\delta \ll 1$ leads to asymptotic predictions at high capillary numbers for the drop thickness, the drop velocity and the additional pressure drop, all fairly well captured by the numerical simulations. Drops with $\lambda < 0.5$, on the other hand, seem to approach, at high capillary numbers, a shape with a non-zero limiting cylindrical radius δ_∞. As a consequence, the additional pressure drop tends to a constant, non-zero value depending linearly on the drop volume, but independent of the interfacial tension between the two phases. The limiting film thickness $h^*_\infty = 1 - \delta_\infty$ has been previously reported in studies of liquid displacement by inviscid gas (Taylor 1961; Cox 1962; Giavedoni & Saita 1997) or by another liquid (Soares *et al.* 2005), but has not been discussed in the context of finite viscous drops.

Since in this case the cylindrical radius δ is bounded away from zero, with δ_∞ as large as $\sqrt{0.4} \approx 0.632$ in the limit $\lambda \to 0$, the infinitely thin drop asymptotics (valid for $\lambda > 1/2$) do not apply. We have not found an asymptotic model appropriate for such low-viscosity drops, but our simulations suggest that the limiting drop thickness and velocity may be approximated by (5.3).

No steady state could be found above a certain critical capillary number Ca_c. Two post-critical behaviours have been identified, depending on which phase is the more viscous. If the drop is more viscous than the suspending fluid ($\lambda > 1$), capillary instabilities appear, grow and eventually saturate owing to the presence of the wall. The drop exhibits periodic oscillations characterized by capillary waves travelling from front to rear. The dimensionless period of the motion increases linearly with Ca, but is independent of the drop size. The critical capillary number decreases rapidly as the drop size or the viscosity ratio increases. Such capillary instabilities have been well studied for infinitely long, annular flows, but have not, to our knowledge, been previously observed or predicted for drops of finite length.

When the drop is less viscous than the suspending fluid ($\lambda < 1$), we find that the characteristic dimple at the rear of the drop eventually turns into a re-entrant jet, leading to burst. The value of Ca_c increases as λ decreases; it becomes independent of the drop size for $\alpha > 1.1$, typically, since the end caps of large drops are independent of the drop volume. The limit film thickness h^*_∞ can be better investigated when considering an infinitely long fluid finger displacing a more viscous liquid (e.g. Soares *et al.* 2005): since the rear of the drop is disregarded, the re-entrant jet instability is not an issue and the capillary number may be increased indefinitely.

A second, companion paper will present results for the streaming potential generated by motion of an uncharged drop in a capillary with charged walls. We finally point out that the flow geometry in porous rock rarely consists of straight capillaries, and there is much still to be done in more realistic geometries.

This work was partially funded by an E.U. Marie Curie fellowship awarded to E.L., contract IEF-041766 (EOTIP).

Note added in proof: the difference between the cases $\lambda < 1/2$ and $\lambda \geqslant 1/2$ has recently been noted independently by Soares & Thompson (2009) in the context of fluid-fluid displacement in a capillary.

REFERENCES

Bai, R., Chen, K. & Joseph, D. D. 1992 Lubricated pipelining: stability of core-annular flow. Part 5. Experiments and comparison with theory. *J. Fluid Mech.* **240**, 97–132.

Brenner, H. 1971 Pressure drop due to the motion of neutrally buoyant particles in duct flows. II. Spherical droplets and bubbles. *Ind. Engng Chem. Fundam.* **10** (4), 537–543.

Bretherton, F. P. 1961 The motion of long bubbles in tubes. *J. Fluid Mech.* **10** (2), 166–188.

Cox, B. G. 1962 On driving a viscous fluid out of a tube. *J. Fluid Mech.* **14** (1), 81–96.

Dupont, J.-B., Legendre, D. & Fabre, J. 2007 Motion and shape of long bubbles in small tube at low Re-number. In *Intl Conf. Multiphase Flow, Leipzig, Germany, July 9–13, 2007*.

Edvinsson, R. K. & Irandoust, S. 1996 Finite-element analysis of Taylor flow. *AIChE J.* **42** (7), 1815–1823.

Giavedoni, M. D. & Saita, F. A. 1997 The axisymmetric and plane cases of a gas phase steadily displacing a Newtonian liquid: a simultaneous solution of the governing equations. *Phys. Fluids* **9** (8), 2420–2428.

Goldsmith, H. L. & Mason, S. G. 1963 The flow of suspensions through tubes: II. Single large bubbles. *J. Colloid Interface Sci.* **18**, 237–261.

Greenstein, T. & Happel, J. 1968 Theoretical study of the slow motion of a sphere and a fluid in a cylindrical tube. *J. Fluid Mech.* **34** (4), 705–710.

Hetsroni, G., Haber, S. & Wacholder, E. 1970 The flow in and around a droplet moving axially within a tube. *J. Fluid Mech.* **41** (4), 699–705.

Ho, B. P. & Leal, L. G. 1975 The creeping motion of liquid drops through a circular tube of comparable diameter. *J. Fluid Mech.* **71** (2), 361–384.

Hodges, S. R., Jensen, O. E. & Rallison, J. M. 2004 The motion of a viscous drop through a cylindrical tube. *J. Fluid Mech.* **501**, 279–301.

Hyman, W. A. & Skalak, R. 1972 Viscous flow of a suspension of liquid drops in a cylindrical tube. *Appl. Sci. Res.* **26**, 27–52.

Joseph, D. D. & Renardy, Y. Y. 1993 *Fundamentals of Two-Fluid Dynamics. Part II: Lubricated Transport, Drops and Miscible Liquids*, 1st ed. Springer.

Lac, E. & Sherwood, J. D. 2009 Streaming potential generated by a drop moving along the centreline of a capillary. *J. Fluid Mech.* (in press) doi:10.1017/S002211200999156X.

Liron, N. & Shahar, R. 1978 Stokes flow due to a Stokeslet in a pipe. *J. Fluid Mech.* **86** (4), 727–744.

Martinez, M. J. & Udell, K. S. 1989 Boundary integral analysis of the creeping flow of long bubbles in capillaries. *J. Appl. Mech.* **56** (1), 211–217.

Martinez, M. J. & Udell, K. S. 1990 Axisymmetric creeping motion of drops through circular tubes. *J. Fluid Mech.* **210**, 565–591.

Olbricht, W. L. 1996 Pore-scale prototypes of multiphase flow in porous media. *Ann. Rev. Fluid Mech.* **28**, 187–213.

Olbricht, W. L. & Kung, D. M. 1992 The deformation and breakup of liquid drops in low Reynolds number flow through a capillary. *Phys. Fluids* A **4** (7), 1347–1354.

Papageorgiou, D. T., Maldarelli, C. & Rumschitzki, D. S. 1990 Nonlinear interfacial stability of core-annular film flows. *Phys. Fluids* A **2** (3), 340–352.

Pozrikidis, C. 1992 *Boundary Integral and Singularity Methods for Linearized Viscous Flow*. Cambridge University Press.

Preziosi, L., Chen, K. & Joseph, D. 1989 Lubricated pipelining: stability of core-annular flow. *J. Fluid Mech.* **201**, 323–356.

Ratulowski, J. & Chang, H.-C. 1989 Transport of gas bubbles in capillaries. *Phys. Fluids* A **1** (10), 1642–1655.

Soares, E. J., Carvalho, M. S. & Souza Mendes, P. R. 2005 Immiscible liquid–liquid displacement in capillary tubes. *J. Fluids Engng* **127**, 24–31.

Soares, E. J. & Thompson, R. L. 2009 Flow regimes for the immiscible liquid-liquid displacement in capillary tubes with complete wetting of the displaced liquid. *J. Fluid Mech.* (accepted for publication) doi:10.1017/S0033223.9991546.

Stone, H. & Leal, L. G. 1989 The influence of initial deformation on drop breakup in subcritical time-dependent flows at low Reynolds numbers. *J. Fluid Mech.* **206**, 223–263.

Taylor, G. I. 1961 Deposition of a viscous fluid on the wall of a tube. *J. Fluid Mech.* **10** (2), 161–165.

Tsai, T. M. & Miksis, M. J. 1994 Dynamics of a drop in a constricted capillary tube. *J. Fluid Mech.* **274**, 197–217.

Westborg, H. & Hassager, O. 1989 Creeping motion of long bubbles and drops in capillary tubes. *J. Colloid Interface Sci.* **133** (1), 135–147.